8217440

Montierth, Leland Melvin

STATIONARY FLOW MODEL OF ABLATIVELY IMPLODED INERTIAL CONFINEMENT FUSION TARGETS

The University of Arizona PH.D. 1982

University
Microfilms
International 300 N. Zeeb Road, Ann Arbor, MI 48106

STATIONARY FLOW MODEL OF ABLATIVELY IMPLODED INERTIAL CONFINEMENT FUSION TARGETS

by

Leland Melvin Montierth

A Dissertation Submitted to the Faculty of the

DEPARTMENT OF NUCLEAR ENGINEERING

In Partial Fulfillment of the Requirements
For the Degree of

DOCTOR OF PHILOSOPHY

In the Graduate College

THE UNIVERSITY OF ARIZONA

1 9 8 2

THE UNIVERSITY OF ARIZONA
GRADUATE COLLEGE

As members of the Final Examination Committee, we certify that we have read the dissertation prepared by Leland Melvin Montierth

entitled Stationary Flow Model of Ablatively Imploded Inertial Confinement Fusion Targets

and recommend that it be accepted as fulfilling the dissertation requirement for the Degree of Doctor of Philosophy.

Dec 29 1981
Date

Dec 25 1981
Date

29 Dec. 1981
Date

29 Dec 1981
Date

Dec 27 '81
Date

Final approval and acceptance of this dissertation is contingent upon the candidate's submission of the final copy of the dissertation to the Graduate College.

I hereby certify that I have read this dissertation prepared under my direction and recommend that it be accepted as fulfilling the dissertation requirement.

Dissertation Director

April 7, 1982
Date

STATEMENT BY AUTHOR

This dissertation has been submitted in partial fulfillment of requirements for an advanced degree at The University of Arizona and is deposited in the University Library to be made available to borrowers under rules of the Library.

Brief quotations from this dissertation are allowable without special permission, provided that accurate acknowledgment of source is made. Requests for permission for extended quotation from or reproduction of this manuscript in whole or in part may be granted by the head of the major department or the Dean of the Graduate College when in his judgment the proposed use of the material is in the interests of scholarship. In all other instances, however, permission must be obtained from the author.

SIGNED: Leland Melvin Monteith

To my father, mother, wife and daughter.

ACKNOWLEDGMENTS

The author would like to acknowledge the support, guidance and direction of Professor Richard L. Morse.

TABLE OF CONTENTS

LIST OF ILLUSTRATIONS

LIST OF ILLUSTRATIONS--Continued

LIST OF ILLUSTRATIONS--Continued

ABSTRACT

The steady flow model is applied to ablatively accelerated spherical targets for inertial confinement fusion. A parameter study is conducted which identifies regions of good hydrodynamic efficiency. In the limit of very large acceleration the model is seen to become planar and can be used to treat some large aspect ratio shells. A model of charged particle beam driven ablation is presented. The ablation resulting from this form of energy deposition can resemble laser driven ablation in some cases, but qualitatively different behavior occurs in certain regimes of the beam power and range. Laser energy deposition by inverse bremsstrahlung is also included. A procedure for descaling the dimensionless results of the steady flow model is presented. This allows for comparison of the model with experiments and numerical simulations.

CHAPTER 1

INTRODUCTION

Most studies of the implosion process of inertial confinement fusion targets by ablation are done with full time-dependent numerical simulation codes. These simulation studies (Nuckolls et al., 1972; Clarke, Fisher, and Mason, 1973) typically involve the modeling of a large number of different physical phenomena. Due to the number of parameters which this introduces, possible difficulties in numerical modeling, and limitations on computer resources, it is often difficult to do thorough parameter studies in order to identify regions of optimum performance. Steady flow models (Fauquignon and Floux, 1970; Bobin, 1971; Brueckner and Jorna, 1974; Gitomer, Morse, and Newberger, 1977; Max, McKee, and Mead, 1976; Felber, 1977) of the ablation process can provide a simple means of doing more thorough parameter studies and of obtaining scaling laws. This information can then be used to direct detailed numerical simulations.

In steady flow models the ablation front is envisioned to be held stationary with material flowing through it. This is depicted in Fig. 1, which presents a brief description of an inertial confinement fusion target. This figure shows a quarter section of a shell-like target. The inner surface of the shell is at $r=r_{s2}$; the inner region of the target is void of material. Since steady flow is assumed there must be a

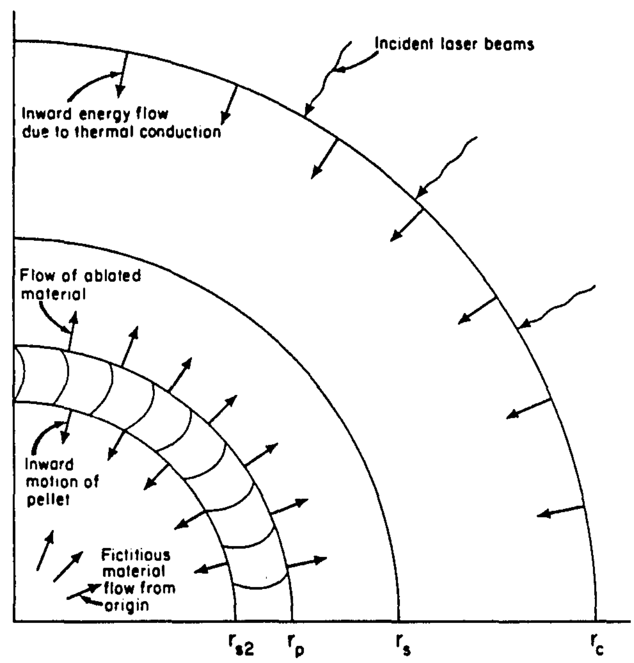

Figure 1. A shell-like inertial confinement fusion target.

This shows the directions of mass flow and heat flow as well as the inward motion of the target.

fictitious flow of material from within this void. Since this is clearly unphysical the steady flow model is not applicable within this region. The material which composes the shell is located between r_{s2} and r_p, the location of the outer pellet surface. The laser energy is assumed to be absorbed at the critical surface, at $r=r_c$, where the plasma frequency is equal to the laser frequency. Energy from the incident laser is transported via thermal conduction to the pellet surface where it drives the ablation. This ablating material generates an inertial reaction pressure which is responsible for the inward acceleration of the target. The flow velocity of the ablated material, or blow-off, is initially subsonic and becomes supersonic due to spherical nozzelling effects. The flow velocity is just sonic at $r=r_s$.

The steady flow model of Gitomer et al. (1977) is used as a starting point for this work. In their model the blow-off is supersonic which correctly models the effects of spherical nozzelling. The energy driving the ablation is from the interaction of laser light with matter and is assumed to be deposited entirely at the critical surface. This energy is then transported to the ablation surface by electron thermal conductivity. They show that due to the boundary condition placed on the temperature in the blow-off region, the critical density, ρ_c (the density at which the laser light is absorbed), must always be less than the sonic density, ρ_s, of the flow. Their model is spherically symmetric and is based on the steady state continuity, momentum and energy equations, where the thermodynamic and flow variables are scaled according to values at the isothermal sonic point. Their results describe the case of no inward acceleration even though the equations of their model include acceleration terms. That is, their results model solid targets since the finite pressure of the material in the center counters the forces due to the ablation pressure, thus preventing significant inward acceleration. Several scaling laws are also given.

The work presented here extends this model to include ablative accelerating targets, deposition of driver energy by charged particle beams, the absorption of laser energy by inverse bremsstrahlung to investigate cases where $\rho_c > \rho_s$, and a procedure for descaling the results.

Accelerating targets are shell-like, with an inner void, and are currently of interest for inertial confinement fusion schemes because they achieve large compressions. Acceleration effects for these targets become significant when they are at least as large as or larger than effects due to spherical convergence. Solutions for this case are thoroughly investigated and regions of good hydrodynamic efficiency are identified.

There are some results shown where thermal conduction plays a very diminished role in inward energy transport. These results occur in the cases of energy deposition by charged particle beams and by inverse bremsstrahlung when $\rho_c > \rho_s$. However in the case of total laser energy deposition at the critical surface the role of thermal conduction is always significant.

The descaled results are presented in such a manner that values of the flow variables at the sonic and critical densities can be found from parameters which the experimenter should readily know.

CHAPTER 2

THE ABLATION MODEL

The steady flow model presented here parallels the model presented in Gitomer et al. (1977) except that some modifications are introduced in order to allow for a more generalized deposition of driver energy.

The Mathematical Model

It is assumed that the flow of material is radially outward, spherically symmetric and stationary. The assumption of stationary flow is valid since in most cases of interest the time necessary to establish flow between the pellet surface and the region where the energy is deposited is much less than the characteristic implosion time. Stationary flow can also be assumed since the forces associated with the pressure gradient in the ablation region are larger than forces associated with the average inward acceleration. For simplicity a single temperature is assumed rather than separate electron and ion temperatures.

The steady state hydrodynamic and energy equations are mass continuity

$$\frac{d}{dr}(\rho v r^2) = 0 \tag{1}$$

momentum balance

$$\rho v \frac{dv}{dr} = - \frac{dP}{dr} - \rho \frac{d\psi}{dr} \tag{2}$$

and energy balance

$$\tfrac{1}{2}v^2 + \frac{\gamma}{\gamma-1} P/\rho + \psi - \frac{a\kappa}{S}\frac{dT}{dr} - \frac{W}{S} = \tfrac{1}{2}v_b{}^2 \qquad (3)$$

where ρ is the fluid mass density, v is the radial fluid velocity, r is the radius, P is the pressure, ψ is the gravitational potential used to model the inward acceleration of shell type targets, $\gamma = 5/3$ is the ratio of specific heats and $v_b{}^2$ is the Bernoulli energy flow constant. This constant represents the energy contribution of incoming fluid from inside the ablation region. The term $(a\kappa/S)(dT/dr)$ is the contribution from thermal conduction in the energy equation. Here $S=4\pi r^2\rho v$ is the mass flow rate, which by Eq. (1) is constant throughout the flow region, $a=4\pi r^2$ is the surface area at r, T is the temperature and κ is the thermal conductivity coefficient given by

$$\kappa = G(Z)\ T^{\alpha}\ \rho^{-\beta}$$

The constants $\alpha = 5/2$, $\beta = 0$, and $G(Z) = \kappa_o/Z$ are given by Spitzer (1962), where κ_o is a constant and Z is the atomic number of the fluid. This simple expression for G(Z) is valid for Z>>1.

The inward energy flow rate is given by W(>0) which represents the flux of incident laser radiation or charged particles. The exact form of W is determined by the choice of driver energy.

The pressure is given by the fully ionized, ideal gas equation of state, $P=R\rho T$, where $R=(1+Z)k/m_i$ and k is the Boltzman constant and m_i is the ion mass, respectively. After manipulating and substitution Eqs. (1), (2) and (3) become

$$\rho v a = S \tag{4}$$

$$v\left(1 - \frac{RT}{v^2}\right)\frac{dv}{dr} = RT\left(\frac{2}{r} - \frac{1}{T}\frac{dT}{dr}\right) - \frac{d\psi}{dr} \tag{5}$$

$$\tfrac{1}{2}v^2 + \frac{\gamma}{\gamma-1}RT + \psi - \frac{a}{S}\kappa\frac{dT}{dr} - \frac{W}{S} = \tfrac{1}{2}v_b{}^2 \tag{6}$$

Since transonic solutions are of interest, the above equations are scaled in the following manner. Define $\tilde{\rho}=\rho/\rho_s$, $\tilde{v}=v/v_s$, $\tilde{r}=r/r_s$, $\tilde{\psi}=\psi/v_s{}^2$, $\tilde{W}=2W/Sv_s{}^2$ and $\tilde{T}=T/T_s$ and ρ_s, v_s and T_s are the flow variables at the isothermal sonic point, r_s; thus at r_s, $v_s=(RT_s)^{\frac{1}{2}}$. With this scaling Eqs. (3), (4) and (5) become

$$\frac{d\tilde{v}}{d\tilde{r}} = \frac{\dfrac{2\tilde{T}}{\tilde{r}} - \dfrac{d\tilde{T}}{d\tilde{r}} - \dfrac{d\tilde{\psi}}{d\tilde{r}}}{\tilde{v}(1 - \tilde{T}\,/\,\tilde{v}^2)} \tag{7}$$

$$\frac{d\tilde{T}}{d\tilde{r}} = M\,\frac{(\tilde{v}^2-\tilde{v}_b{}^2)/2+\eta\tilde{T}+\tilde{\psi}-\tilde{W}/2}{\tilde{r}^2\,\tilde{T}^2} \tag{8}$$

where $\eta = \gamma/(\gamma-1)$. The quantity M is defined as

$$M = \frac{r_s\rho_s v_s{}^3}{\kappa_s T_s} = \frac{r_s\rho_s v_s{}^3}{G(Z)T_s{}^{1+\alpha}} = \frac{r_s\rho_s R^{1+\alpha}v_s{}^{1-2\alpha}}{G(Z)} = \frac{r_s\rho_s R^{3/2}}{G(Z)T_s{}^{\alpha-\frac{1}{2}}} \tag{9}$$

where as before the subscript s refers to quantities at the sonic point, r_s.

The inward acceleration potential, ψ, corresponds to an outward directed gravity by $g = -d\psi/dr$. While having g increase with r in order to account for decreasing convergence effects might better model the high density region of the shell, this would prove unsatisfactory in the lower density region as r increases further. As a compromise, a constant value of g is chosen and ψ is of the form, $\psi=g(r_s-r)$. This is scaled such that $\tilde{g}=gr_s/v_s^2$ and $\tilde{\psi}=\tilde{g}(1-\tilde{r})$.

The critical surface is defined as being where the plasma frequency is equal to the frequency of the incident laser light. This occurs at $r=r_c$ and $\rho=\rho_c$. For the case of total laser energy deposition at the critical radius, r_c, W increases discontinuously from zero to W_∞, the power of the incident laser, i.e.

$$\begin{aligned} W &= 0 \quad , & r &< 0 \\ W &= W_\infty \quad , & r &\geqslant r_c \end{aligned} \tag{10}$$

This case is subsequently referred to as the laser deposition case. A simplified energy range relationship for a monoenergetic beam of particles is used for the case of the charged particle beam

$$\frac{dW}{dr} = \frac{\rho}{\sigma_\infty} \; \frac{W_\infty^2}{W} \tag{11}$$

where σ_∞ is the range in units of mass per unit area of the incident beam and W_∞ is the power of the beam as $r \to \infty$. In this case the beam emerges with power W_∞ and is attenuated until $W \to 0$ at $r=r_R$. A more sophisticated relationship including temperature dependence or multi-energy particles could replace Eq. (11), but the essential phenomena can be modeled by this relationship. When scaled, Eqs. (10) and (11) become

$$\tilde{W} = 0 \qquad , \quad \tilde{r} < \tilde{r}_c$$
$$= \tilde{W}_\infty \qquad , \quad \tilde{r} \geqslant \tilde{r}_c \tag{12}$$

$$\frac{d\tilde{W}}{d\tilde{r}} = \frac{\tilde{\rho}\,\tilde{W}_\infty^{\,2}}{\tilde{\sigma}_\infty\,\tilde{W}} \quad , \quad \tilde{r} \geqslant \tilde{r}_R \tag{13}$$

for laser deposition and for charged particle beams, respectively, where $\tilde{\sigma}_\infty = \sigma_\infty/\rho_s r_s$. While inverse bremsstrahlung is a mechanism by which laser energy is deposited, its deposition model is more like that of the charged particle beam. This model is presented in Appendix A.

Solution Considerations and Parameter Limits

Numerical solutions of Eqs. (7), (8) and (12) or (13) are obtained most easily by integrating outwards ($\tilde{r} > 1$) and inwards ($\tilde{r} < 1$) from the isothermal sonic point (i.e., $\tilde{r}$=1). Since $\tilde{v}=\tilde{T}=1$ at this point Eq. (7) is singular, and in order that $d\tilde{v}/d\tilde{r}$ be finite, (to insure continuous solutions) the numerator must also vanish. This requires that

$$\left.\frac{d\tilde{T}}{d\tilde{r}}\right|_{\tilde{r}=1} = 2 - \left.\frac{d\tilde{\psi}}{d\tilde{r}}\right|_{\tilde{r}=1} \tag{14}$$

which is equivalent to Eq. (8) at $\tilde{r}$=1. An expression for M is then derived

$$M = \frac{2(2+\tilde{g})}{1 - \tilde{v}_b^{\,2} + 2\eta - \tilde{W}_s} \tag{15}$$

where $\tilde{W}_s$ is the value of $\tilde{W}$ at $\tilde{r}=\tilde{r}_s=1$. This value is in general nonzero except for the case of total energy deposition at the critical radius.

Equation (15) relates M and $\tilde{v}_b^2$ for a given choice of the other parameters. The value of the velocity derivative at the singularity must be found by applying l'Hospital's rule, in which case

$$\left.\frac{d\tilde{v}}{d\tilde{r}}\right|_{\tilde{r}=1} = \frac{1}{4}\left[-B + (B^2-8C)^{\frac{1}{2}}\right] \tag{16}$$

where

$$B = M - (2+\tilde{g})$$

$$C = (2+\tilde{g})\left[M\eta-4-\alpha(2+\tilde{g})\right] - \frac{M\tilde{W}_\infty^{\,2}}{2\tilde{W}_s\tilde{\sigma}_\infty} + 2$$

Also, this value must be greater than zero since supersonic solutions are desired for $\tilde{r} > 1$ and subsonic solutions for $\tilde{r} < 1$. This requires that $C < 0$ in Eq. (16). This places an upper limit on $\tilde{v}_b^2$. A lower limit is found by reference to Eq. (3). If at the pellet surface (i.e., at $\tilde{r}=\tilde{r}_p$), the net energy of the flow approaches zero, i.e., $v \rightarrow 0$, $\rho \rightarrow \infty$ and $\kappa \rightarrow 0$ since $T \rightarrow 0$; then the lower limit of $\tilde{v}_b^2$ is

$$\tilde{v}_b^2/2 > \left.\tilde{\psi}\right|_{\tilde{r}=\tilde{r}_p} \equiv \tilde{g}(1-\tilde{r}_p) \tag{17}$$

which corresponds to the potential difference between the pellet surface and the sonic point. For $\tilde{g}=0$ the lower limit of $\tilde{v}_b^2$, $\tilde{v}_{b\ell}^2$, is zero and for $\tilde{g} > 0$ it is given by Eq. (17). Since $\tilde{r}_p$ is not known a priori to solving Eqs. (7), (8) and (12) or (13), an estimate of $\tilde{v}_{b\ell}^2$ is found by choosing a value of $\tilde{v}_b^2$ for a given $\tilde{g}$ which gives a solution and then solving Eq. (17). Thus the limits of $\tilde{v}_b^2$ are

$$2\tilde{g}(1-\tilde{r}_p) < \tilde{v}_b{}^2 < 1+2\left\{\eta-\tilde{W}_s/2 - \frac{(2+\tilde{g})\left[2\eta+\tilde{g}(\eta-1) - \frac{\tilde{W}_\infty^2}{2\tilde{\sigma}_\infty\tilde{W}_s}\right.}{(2+\tilde{g})\left[4+\alpha(2+\tilde{g})\right] - 2}\right\} \tag{18}$$

For $\tilde{g}=0$, $\tilde{W}_s=0$, $\alpha=5/2$ and $\eta=5/2$ the limits are $0<\tilde{v}_b{}^2<19/4$. For $\tilde{g}=1$ or $\tilde{g}=\infty$ and the same choices as before, $\tilde{v}_b{}^2 < 24/5$. These larger values of $\tilde{v}_b{}^2$ represent cases in which the convective energy flow from within the pellet constitutes a large percentage of the total energy flow through the sonic point. These cases are not of physical interest and best correspond to burn through which results in very poor compression.

The upper limit values of $\tilde{v}_b{}^2$ are of interest in charged particle beam cases when $\tilde{W}_s > 0$. For increasing values of $\tilde{W}_s$ the upper limit value of $\tilde{v}_b{}^2$ approaches zero (refer to Eq. 18). This corresponds to M ->∞, i.e., the denominator of Eq. (15) approaches zero. Since M is a dimensionless ratio of physical parameters it must be greater than zero, thus from Eq. (15)

$$\tilde{W}_s \leqslant 2\eta + 1 - \tilde{v}_b{}^2 \tag{19}$$

and the largest value for $\tilde{W}_s$ is found by replacing $\tilde{v}_b{}^2$ with $\tilde{v}_{b\ell}^2$. For $\tilde{g}=0$ and $\eta=5/2$ this value is $\tilde{W}=6$. Inspection of Eq. (9) shows that M ->∞ corresponds to κ_s ->0, and thus thermal conduction plays a very diminished role. All inward energy flow is transported by the beam. The energy of the incoming particle beam is converted directly to convective energy.

Solution Characteristics

As outlined in Gitomer et al. (1977) for the case of laser deposition, W_∞, the power of the incident laser is adjusted such that $T \to 0$ as $r \to \infty$. Thus for $r > r_c$, $dT/dr<0$, but at $\tilde{r}=1$, $dT/dr>0$. This restricts r_c to values as large as or larger than r_s, i.e., $\tilde{r}_c \geqslant 1$. Likewise the critical density, ρ_c, must be smaller than ρ_s.

Solution Intervals

For the laser deposition case there are four distinguishable regions in $\tilde{r}$. These regions can also be seen by referring back to Fig. 1. The regions are:

(1) $\tilde{r}_{s2} < \tilde{r} < \tilde{r}_p$; $\tilde{r}_{s2}$ is the location of a second sonic point at which the stationary flow model is no longer applicable. $\tilde{r}_p$ is chosen at the point $d\tilde{v}/d\tilde{r}=0$ and coincides with the pellet surface. In this region heat flow plays an unimportant role since the conductivity is so small.

(2) $\tilde{r}_p < \tilde{r} < 1$; this is the subsonic portion of the ablation front.

(3) $1 < \tilde{r} < \tilde{r}_c$; this is the supersonic portion of the ablation front and $d\tilde{T}/d\tilde{r} > 0$.

(4) $\tilde{r}_c < \tilde{r} < \infty$; the flow is supersonic and $d\tilde{T}/d\tilde{r} < 0$. As $\tilde{r} \to \infty$, $\tilde{T} \to 0$ and $\tilde{v} \to \tilde{v}_\infty$, where $\tilde{v}_\infty$ is the ablation exhaust velocity, which is finite for $\tilde{g}=0$. For $\tilde{g}$=a constant$\neq 0$, $\tilde{v}_\infty$ approaches infinity and $\tilde{v}_\infty$ is not specified.

Asymptotic solutions are given in Gitomer et al. (1977) for region (3) for $\tilde{r}_c \to \infty$ and for region (4) which indicate that $\tilde{T} \to 0$ is the proper boundary condition as $\tilde{r} \to \infty$.

For the case of charged particle beam deposition, there are also four distinct regions. When $\tilde{W}_s=0$ these regions correspond to those of the laser case except that $\tilde{r}_c$ is replaced by $\tilde{r}_R$, the point at which $\tilde{W} \to 0$. Also, the boundary condition of region (4) is satisfied by adjusting the quantity $\tilde{W}_\infty^2/\tilde{\sigma}_\infty$ in Eq. (13). Integration of this equation gives $\tilde{W} \to \tilde{W}_\infty$ as $\tilde{r} \to \infty$, which determines $\tilde{\sigma}_\infty$ since $\tilde{W}_\infty^2/\tilde{\sigma}_\infty$ is known.

Asymptotic Solutions and Determination of Boundary Conditions

Asymptotic solutions for region (4) similar to those of Gitomer et al. (1977) are given

$$\tilde{v}^2 = \tilde{v}_\infty^2 + \tilde{v}_m^2\,\tilde{r}^m \quad , \quad \tilde{v}_m^2 < 0 \tag{20}$$

$$\tilde{T} = \tilde{T}_m\,\tilde{r}^m \quad , \quad \tilde{T}_m > 0 \tag{21}$$

$$\tilde{W} = \tilde{W}_\infty + \tilde{W}_m\,\tilde{r}^{-1} \quad , \quad \tilde{W}_m < 0 \tag{22}$$

where

$$m = -\frac{1}{1+\alpha}$$

$$\tilde{T}_m = \left[\frac{M(\tilde{v}_\infty^2 - \tilde{v}_b{}^2 - \tilde{W}_\infty)}{2m}\right]^{\frac{1}{1+\alpha}}$$

$$\tilde{v}_m{}^2 = \frac{2(2-m)}{m}\,\tilde{T}_m$$

$$\tilde{W}_m = -\frac{\tilde{W}_\infty}{\tilde{v}_\infty{}^2\,\tilde{\sigma}_\infty}$$

and $\tilde{W}_\infty$ and $\tilde{v}_\infty$ are determined from the integration.

For $\widetilde{W}_s > 0$ only region (1) remains unchanged, region (2) now spans $\widetilde{r}_p < \widetilde{r} < \widetilde{r}_R$, region (3) is $\widetilde{r}_R < \widetilde{r} < 1$ and finally region (4) is $\widetilde{r} > 1$. The boundary conditions of region (4) still apply, but the solution method is modified. It becomes necessary to choose a value of $\widetilde{W}_s$ consistent with Eq. (19) for the given value of $\widetilde{v}_b{}^2$. Again, the ratio $\widetilde{W}_\infty^2/\widetilde{\sigma}_\infty$ is adjusted to give $\widetilde{T} \to 0$ as $\widetilde{r} \to \infty$. $\widetilde{W}_\infty$ is found from the integration. For cases in which thermal conduction is negligible (i.e., $M \to \infty$), $\widetilde{r}_R \to \widetilde{r}_p$ and region (2) becomes increasingly small. Thus the beam is seen to penetrate right up to the ablation front providing the driver energy.

The Acceleration

The inward acceleration of the pellet corresponds to an outwardly directed gravity which is represented by g in the model. In the implosion of solid pellets, $\widetilde{g}$ is zero since the internal pressure of the fuel does not allow for inward acceleration. This case is presented in Gitomer et al. (1977). Values of $\widetilde{g}$ between zero and infinity correspond to differing thicknesses of spherical shells. For very small $\widetilde{g}$ the spherical divergence term, $2\widetilde{T}/\widetilde{r}$, in the momentum equation (Eq. 7) dominates the acceleration term (recall that $\widetilde{g}=d\widetilde{\Psi}/d\widetilde{r}$). As $\widetilde{g}$ is increased further and further acceleration effects become more important than divergence effects.

In the limit of $\widetilde{g} \to \infty$ the spherical divergence corrections in Eqs. (7) and (8) are no longer present and the system becomes planar

$$\frac{d\tilde{v}}{d\tilde{x}} = -\frac{\frac{d\tilde{T}}{d\tilde{x}} - \frac{d\tilde{\psi}}{d\tilde{x}}}{\tilde{v}(1 - \tilde{T}/\tilde{v}^2)} \tag{23}$$

$$\frac{d\tilde{T}}{d\tilde{x}} = M\,\frac{(\tilde{v}^2-\tilde{v}_b{}^2)/2+\eta\tilde{T}+\tilde{\psi}-\tilde{W}/2}{\tilde{T}^{\alpha}} \tag{24}$$

$$M = \frac{x_g\ \rho_s\ v_s{}^3}{\kappa_s\ T_s} \tag{25}$$

where the scaling length $x_g=v_s{}^2/g$ and the isothermal sonic point occurs at $\tilde{x}=0$. To give constant acceleration the gravitational potential is chosen to be $\psi = -gx$, and upon scaling $\tilde{\psi} = -\tilde{x}$ and $d\tilde{\psi}/d\tilde{x} = -1$. In order that $d\tilde{v}/d\tilde{x}$ be finite at $\tilde{x}=0$, where $\tilde{v}=\tilde{T}=1$, the numerator of Eq. (23) must be identically zero. This is satisfied by $d\tilde{T}/d\tilde{x}=1$ and the resulting relationship between M and $\tilde{v}_b{}^2$ is

$$M = \frac{2}{1 - \tilde{v}_b{}^2 + 2\eta-\tilde{W}_s}$$

and the limits of $\tilde{v}_b{}^2$ are

$$2|\tilde{x}_p| < \tilde{v}_b{}^2 < 1 + 2\left[\eta - \frac{\tilde{W}_s}{2} - \frac{\eta-1 - \dfrac{\tilde{W}_\infty^2}{2\tilde{\sigma}_\infty \tilde{W}_s}}{\alpha}\right]$$

CHAPTER 3

DIAGNOSTICS AND PARAMETER DEPENDENCE

Means of evaluating the performance of implosions as well as other diagnostics are introduced. These are useful in relating the results of the steady flow model to experiment and simulation.

Implosion Performance

Further information which relates the results from the steady flow model to physical parameters and gives a measure of performance of the implosion process is developed. One useful quantity is the mass of the pellet, m_p, which is found by integration of the following

$$m_p = \int_{r_{s2}}^{r_p} 4\pi r^2 \rho dr \tag{26}$$

which is solved simultaneously with Eqs. (7), (8) and (12) or (13). The choice of the lower limit of this integral at r_{s2}, near where the model breaks down, is reasonable as long as the pressure at this point is sufficiently less than the ablation pressure, $\tilde{P}_p$. Further discussion of the model's validity is deferred to the next chapter. In general the upper limit of the integral is replaced with a value of r and when scaled, Eq. (26) becomes

$$\tilde{m}(\tilde{r}) = \int_{\tilde{r}_{s2}}^{\tilde{r}} \tilde{r}^2 \tilde{\rho} d\tilde{r} \tag{27}$$

where $\tilde{m}=m/4\pi\rho_s r_s^3$. The following convention is used

$$\tilde{m}_p = \tilde{m}(\tilde{r}_p); \qquad \tilde{m}_s = \tilde{m}(\tilde{r}_s)$$

where $\tilde{m}_s$ is the sum of the mass of the pellet and of the subsonic, ablated material.

Now if the pellet is treated as a sheet mass, its thickness Δr is found from the following

$$\Delta r = \frac{m_p}{4\pi r_p^2 \rho_p} \quad ; \quad \Delta\tilde{r} = \frac{\tilde{m}_p}{\tilde{r}_p^2 \tilde{\rho}_p} \tag{28}$$

where $\Delta\tilde{r}$ is the dimensionless shell thickness. For spherical shells, i.e., $0 < g < \infty$, an aspect ratio, A, is defined in the normal fashion

$$A = \frac{r_p}{\Delta r} = \frac{\tilde{r}_p}{\Delta\tilde{r}} = \frac{\tilde{r}_p^3 \tilde{\rho}_p}{\tilde{m}_p} \tag{29}$$

It is remembered that this is the inflight aspect ratio and not the pellet's initial aspect ratio.

As a means of evaluating the implosion performance, a mass removal coefficient, B, is defined

$$B \equiv \frac{\Delta m}{m_p} = \frac{S\Delta t_I}{m_p} \tag{30}$$

where Δm is the mass removed by ablation as the shell implodes and Δt_I is the characteristic implosion time. It is recalled that $S=4\pi r^2\rho v$ is the mass flow rate. The characteristic implosion time is found by solving the equation of motion to give

$$\Delta t_I = \left(\frac{2r_p}{g}\right)^{\frac{1}{2}} \tag{31}$$

where it is assumed that the shell is accelerated with an acceleration, g, through a distant r_p. This is an approximate time since it neglects the decreasing shell mass as material is ablated and neglects the decrease in acceleration as material converges at the origin. Substituting Eq. (31) into Eq. (30) and scaling gives

$$B = \frac{1}{\tilde{m}_p}\left(\frac{2\tilde{r}_p}{\tilde{g}}\right)^{\frac{1}{2}} \tag{32}$$

Efficient transfer of energy requires that as much mass as possible be removed and yet have sufficient material remaining to be compressed. As in analogy with a rocket-model (the pellet is like a spherical rocket which burns over its entire surface and "travels" inward) the maximum energy transfer from the absorbed laser energy to the final kinetic energy of the pellet occurs when the final mass of the pellet is roughly 1/e times its initial mass (Brueckner, 1974). In terms of B this corresponds to $B=1-1/e=0.63$. Due to the various approximations taken in the definition of Δt_I the optimal range of values for B will be taken to be $0.5 < B < 1$. For larger values of B it is taken that the ablation rate is too large and either too little fuel for efficient transfer of energy or no fuel remains and the pellet burns through.

Parameter Dependence

The family of solutions for both the laser deposition and charged partical beam cases is formed of three parameters. For the former they are $\tilde{v}_b^2$, $\tilde{g}$, and $\tilde{\rho}_c$ and for the latter $\tilde{v}_b^2$, $\tilde{g}$, $\tilde{r}_R$. While the dimensionless parameter M is determined by the values of various physical quantities at the sonic point, its allowable range of values changes with each different choice of $\tilde{g}$. Reference to Eq. (18) shows that this is also true for $\tilde{v}_b^2$. Thus using either of these quantities would be difficult when comparing cases for different values of $\tilde{g}$. For this reason $\tilde{v}_b^2$ is replaced by the scaled density at the pellet surface, $\tilde{\rho}_p$, which is found by the solution procedure. This is a particularly good choice, since this parameter is more readily related to results from experiments or numerical simulations.

CHAPTER 4

RESULTS

The results from the steady flow model are found by numerically solving Eqs. (7), (8) and (12) or (13). Energy deposition is taken to occur at $\tilde{r}=\tilde{r}_c$ unless otherwise indicated. Results are presented for solid pellets: $\tilde{g}=0$; spherical shells, $0 < \tilde{g} < \infty$; and planar targets, $\tilde{g} \rightarrow \infty$. For each value of $\tilde{g}$, solutions are found by varying $\tilde{v}_b^2$ over its range as given by Eq. (18). For the planar case Eqs. (23) and (24) are substituted for Eqs. (7) and (8).

$\tilde{g} = 0$

Figures 2 and 3 present the case $\tilde{\rho}_p=10^2$ for several values of $\tilde{\rho}_c$ plotted linearly and logarithmically, respectively. Logarithmic plots are helpful since scaling laws relating the flow variables to the spatial coordinate can be readily identified. The location of the second sonic point, $\tilde{r}_{s2}$, is at $\tilde{r}=.305$. It is in this region that the steady flow approximation is not valid. A similar case but with $\tilde{\rho}_p=10$ is given in Fig. 4 for comparison. While the supersonic profiles (i.e., $\tilde{r} > 1$) for these two cases are very similar, the subsonic solutions ($\tilde{r} < 1$) bear little resemblance. The latter case corresponds to a larger value of $\tilde{v}_b^2$ and approaching the burn through limit. The next plot, Fig. 5, contains values of the flow variables at the pellet surface as well as M and $\tilde{v}_b^2$ plotted as a function of $\tilde{\rho}_p$. It is noted that for $\tilde{\rho}_p \gtrsim 10$ $\dot{\tilde{r}}_p$, $\tilde{P}_p$ and M

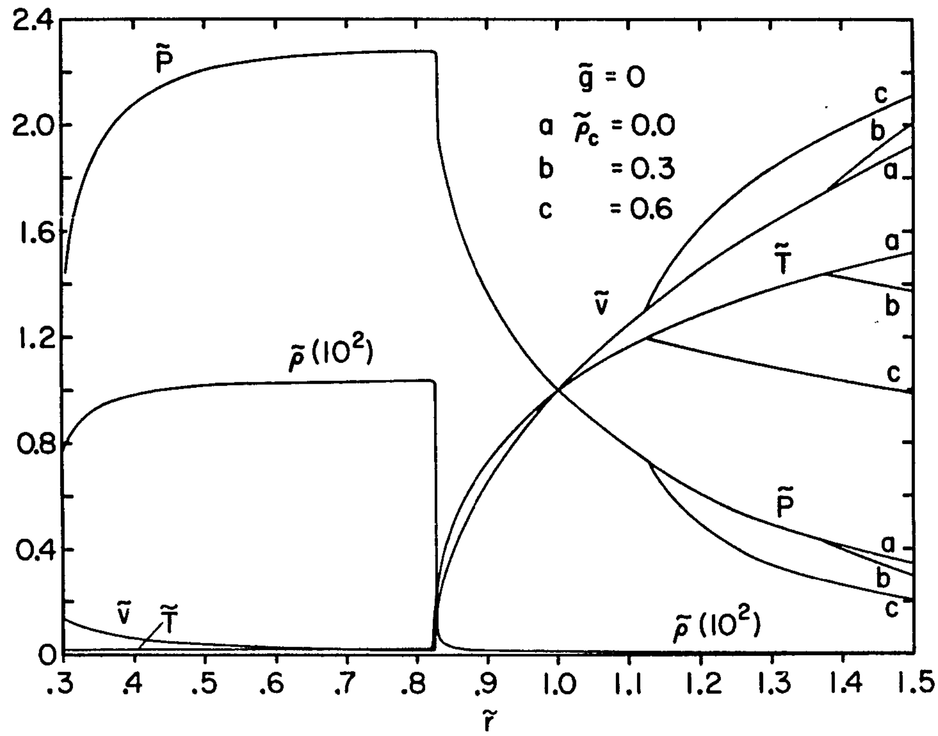

Figure 2. Profiles of the pellet and ablation region for $\tilde{\rho}_p=10^2$ and $\tilde{g}=0$ for several values of $\tilde{\rho}_c$.

The second sonic point, $\tilde{r}_{s2}$, is at $\tilde{r}=.305$. The number in parenthesis following the symbol of the plotted variable is the quantity per unit value of the graph's scale.

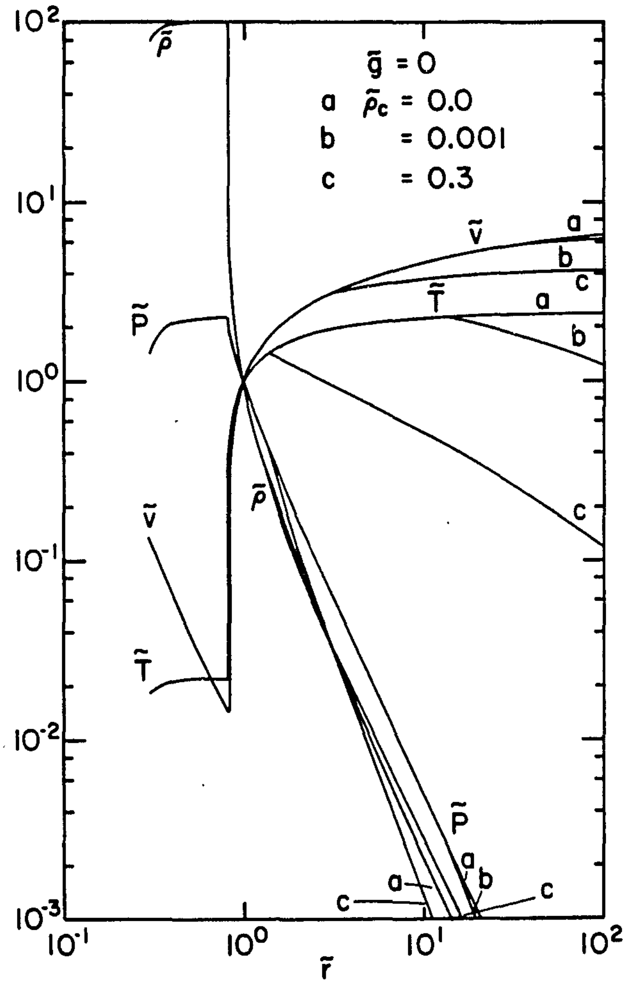

Figure 3. Logarithmic profiles for the case $\tilde{\rho}_p=10^2$, $\tilde{g}=0$ for a range of values of $\tilde{\rho}_c$.

Logarithmic plots are useful since scaling laws are readily seen.

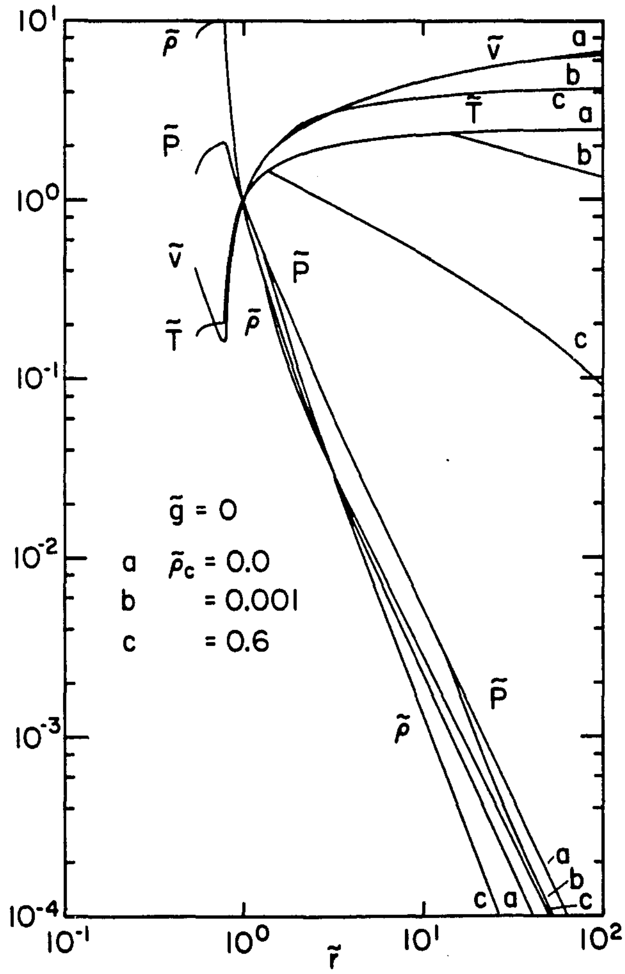

Figure 4. Logarithmic profiles for the comparison case of $\tilde{\rho}_p$=10 and $\tilde{g}$=0.

The subsonic solutions bear little resemblance to the previous case, and it is representative of cases which are approaching the burn through limit.

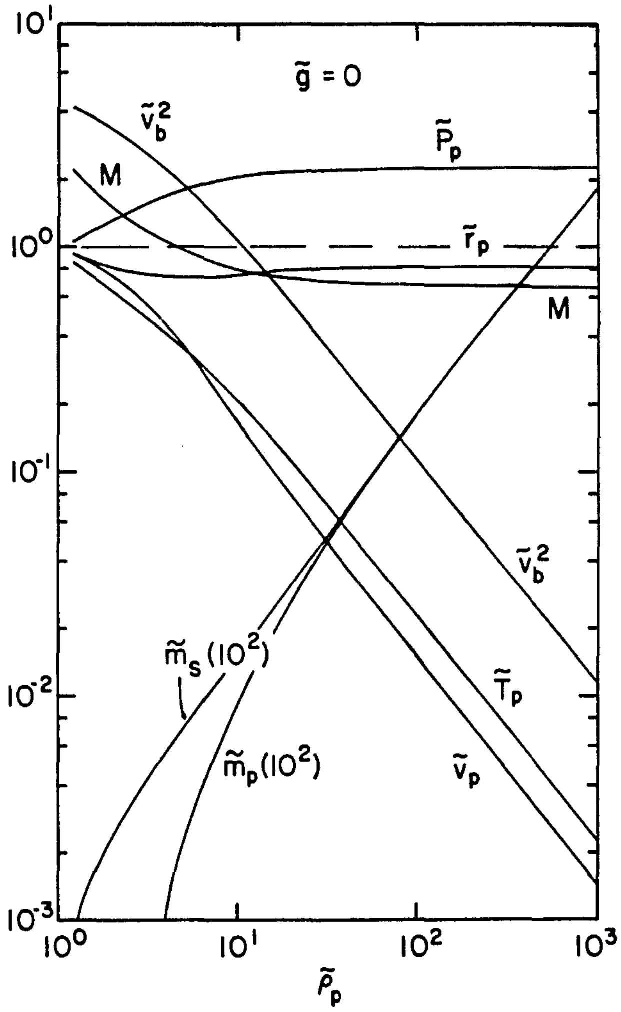

Figure 5. Flow variables at the pellet surface, $\tilde{v}_b^{\,2}$ and M as a function of $\tilde{\rho}_p$ for $\tilde{g}=0$.

Note that $\tilde{r}_p$, $\tilde{P}_p$ and M are nearly constant for $\tilde{\rho}_p > 10$.

are nearly constant; that the amount of mass in the subsonic ablation region, i.e., between $\tilde{r}_p$ and $\tilde{r}_s$, is a small fraction of the pellet's mass, $\tilde{m}_p$, and is nearly proportional to $\tilde{\rho}_p$. Figure 6 gives values at the critical surface, i.e., $\tilde{r}=\tilde{r}_c$, and the deposited power, $\tilde{W}_\infty$, as functions of $\tilde{\rho}_c$. This plot is very similar to Fig. 2(b) of Gitomer et al. (1977) except that it includes the exhaust velocity, $\tilde{v}_\infty$. These quantities are seen to be very weak functions of $\tilde{\rho}_p$ except near $\tilde{\rho}_c$=1. It is seen that $\tilde{W}_\infty$ is proportional to $\tilde{\rho}_c^{-\frac{1}{2}}$ (or to the laser wavelength, λ) which has also been verified by numerical simulation (McCrory and Morse, 1977). If the only means of energy transport away from the pellet is by convection then energy conservation requires that $\tilde{W}_\infty = \tilde{v}_\infty^2 - \tilde{v}_b{}^2$. Since for most cases of interest $\tilde{v}_b{}^2 << \tilde{v}_\infty^2$ then $\tilde{W}_\infty \cong \tilde{v}_\infty^2$. This is clearly not the case for $\tilde{\rho}_c \to 0$ since $\tilde{W}_\infty \alpha \tilde{\rho}_c^{-\frac{1}{2}}$ while $\tilde{v}_\infty^2$ increases much more slowly with decreasing $\tilde{\rho}_c$. Inspection of the asymptotic solutions for $\tilde{r} \to \infty$ of Gitomer et al. (1977) shows there is a finite outward energy flow due to thermal conduction which must be included in the energy conservation requirements. For larger $\tilde{\rho}_c$ it is seen that the condition $\tilde{W}_\infty \cong \tilde{v}_\infty^2 - \tilde{v}_b{}^2$ is satisfied and the deposited laser energy is directly converted to convective energy with outward heat flow being less important.

$\underline{0 < \tilde{g} < \infty}$

Examination of Eq. (7) gives a quick comparison of the effects of spherical divergence and acceleration in the ablation region. The terms $2\tilde{T}/\tilde{r}$ and $\tilde{g}$ (recall that $d\tilde{\psi}/d\tilde{r}=-\tilde{g}$) are the contributions due to

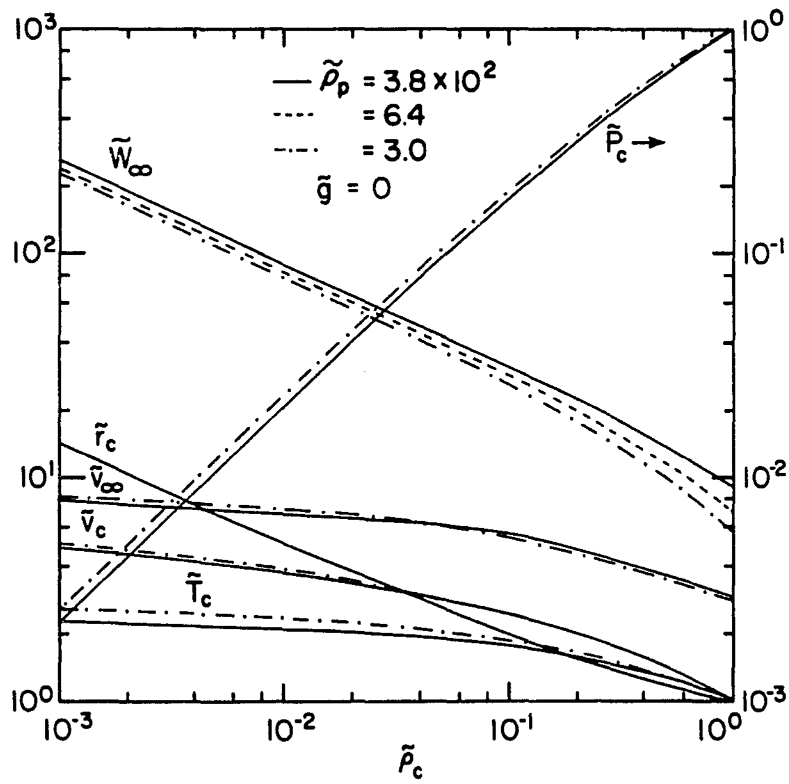

Figure 6. Scaled laser power and flow variables at the critical surface as a function of $\tilde{\rho}_c$ for $\tilde{g}$=0.

The exhaust velocity, $\tilde{v}_\infty$, is also included.

spherical divergence and acceleration, respectively. In the subsonic ablation region the first term assumes the range of $0 < 2\tilde{T}/\tilde{r} \leqslant 2$. This is comparable to a value of acceleration of order 1, i.e., $\tilde{g} \cong 1$. For values of $\tilde{g}$ of order 1 and less than 1, the spherical effect of divergence is at least as important as or dominates the acceleration effect. Thus for any of these values of $\tilde{g}$ the effect of spherical divergence is important in determining values of the various flow quantities at the ablation surface.

Figures 7 and 8 are linear and logarithmic plots of the case $\tilde{\rho}_p=10^2$ and $\tilde{g}=1$ for various values of $\tilde{\rho}_c$. The shell like structure of the pellet is noted; the second sonic point occurs at $\tilde{r}_{s2}=0.85$. This point is taken to be the inner surface of the shell. Figure 9 shows quantities at the pellet surface as a function of $\tilde{\rho}_p$. This plot is similar to Fig. 5 except that the ratio of the distance between the pellet surface and the sonic point to the shell's thickness, $(\tilde{r}_s - \tilde{r}_p)/\Delta\tilde{r}$, is included. This ratio allows comparison with the planar case since an aspect ratio is not defined for this case. The effect of varying $\tilde{g}$ on parameters at the pellet surface is seen in the next two plots. Figures 10 and 11 are for $\tilde{g}=10^{-1/2}$ and $10^{+1/2}$, respectively. Comparison of these plots show that for increasing $\tilde{g}$ the ratio $(\tilde{r}_s - \tilde{r}_p)/\Delta\tilde{r}$ increases, the amount of mass which composes the pellet, $\tilde{m}_p$, decreases, while the amount of mass in the subsonic ablation region increases. While the ratio $(\tilde{r}_s - \tilde{r}_p)/\Delta\tilde{r}$ increases with increasing $\tilde{g}$, it is seen that the distance $(\tilde{r}_s - \tilde{r}_p)$ decreases, implying that $\Delta\tilde{r}$ decreases with increasing $\tilde{g}$. For larger values of $\tilde{g}$ and thus thinner shells, an equation of motion can be written by

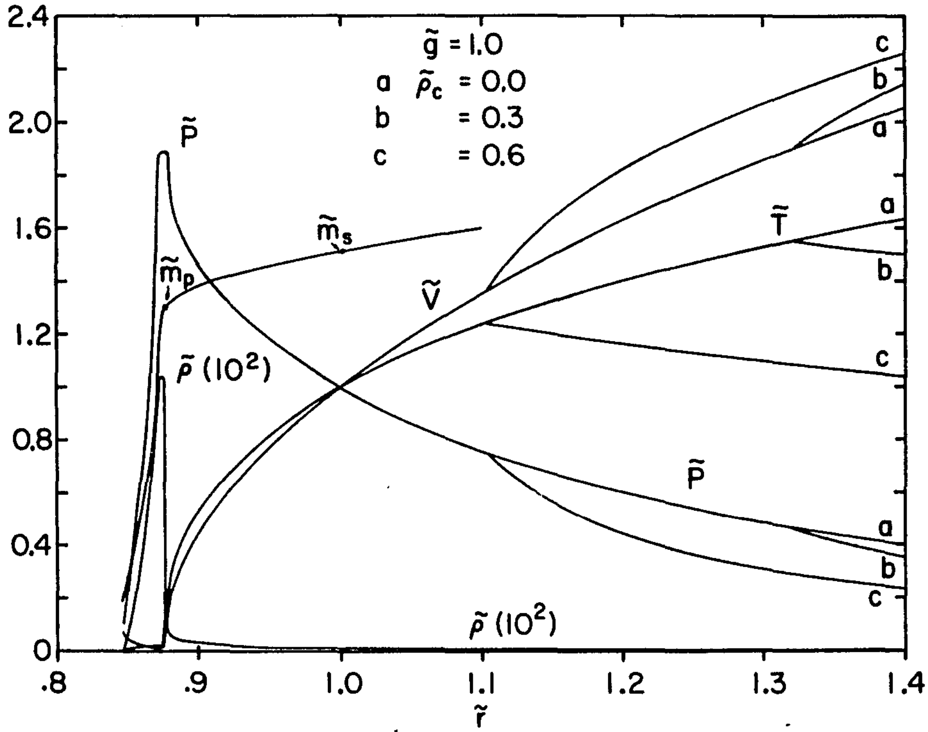

Figure 7. Linear plots of pellet and ablation region for $\tilde{\rho}_p = 10^2$ and $\tilde{g}=1$.

Note the shell-like structure of the pellet. The second sonic point occurs at $\tilde{r}_{s2}=.85$, which is also taken to be the inside surface of the shell.

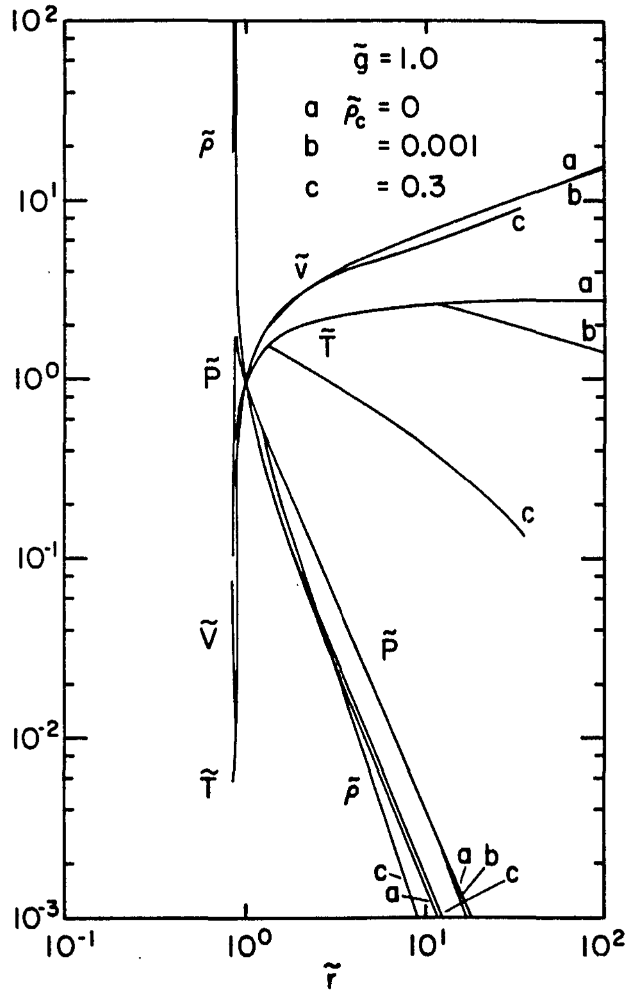

Figure 8. Logarithmic profiles of the laser case with $\tilde{\rho}_p = 10^2$ and $\tilde{g}=1$ for several values of $\tilde{\rho}_c$.

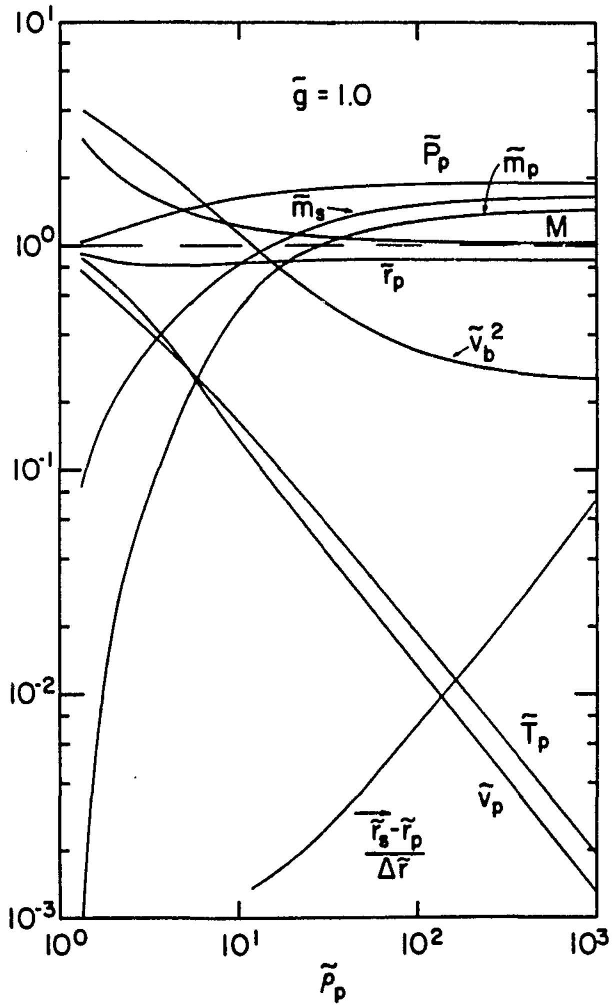

Figure 9. Various quantities associated with the pellet as a function of $\tilde{\rho}_p$ for $\tilde{g}$=1.

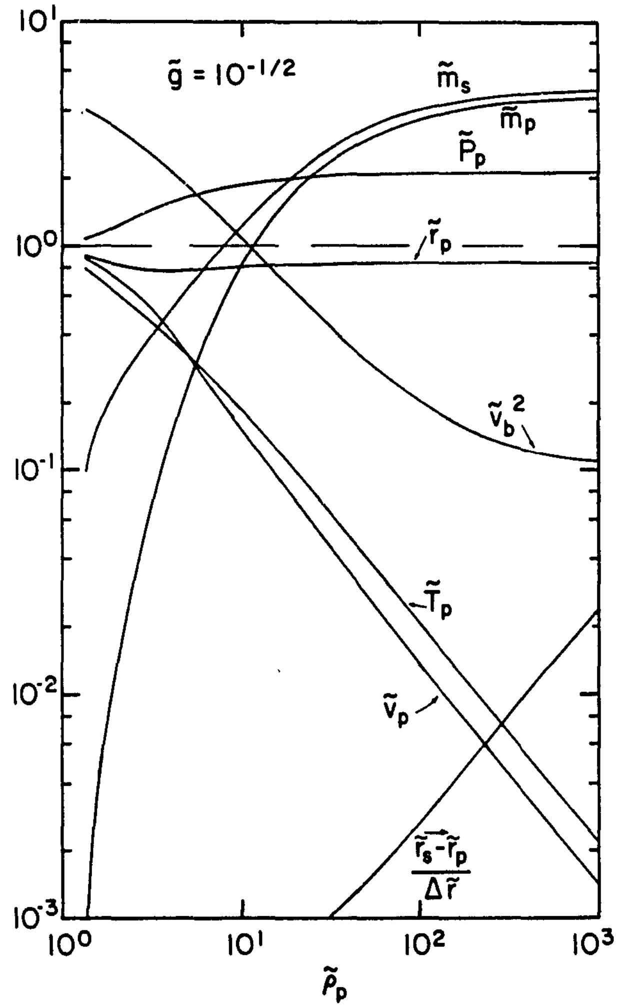

Figure 10. Various scaled quantities evaluated at the pellet surface and sonic point for $\tilde{g}=10^{-\frac{1}{2}}$.

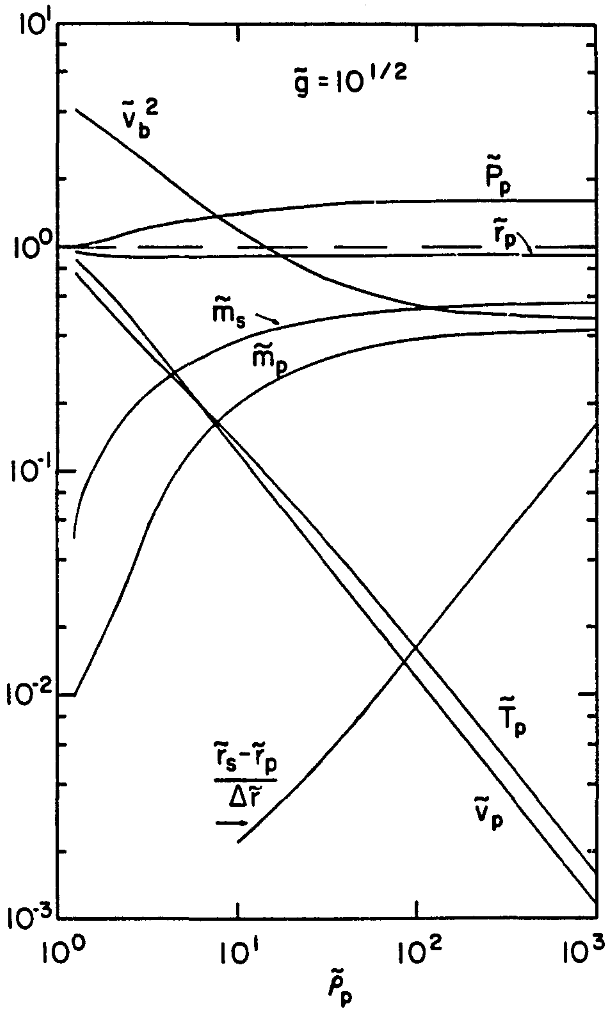

Figure 11. Scaled quantities at the pellet surface and sonic point for $\tilde{g}=10^{+1/2}$.

assuming the shell to be a sheet mass

$$m_p g = 4\pi r_p{}^2 P_p \qquad (33)$$

where the right hand side of the equation represents the force responsible for the inward acceleration, g. Scaling and solving for $\tilde{P}_p$ gives

$$\tilde{P}_p = \frac{\tilde{m}_p \; \tilde{g}}{\tilde{r}_p{}^2} \qquad (34)$$

which is verified by substitution from any of Figs. 9, 10 or 11. Figure 12 gives values at the critical surface as well as the power necessary to drive the ablation for two widely differing values of $\tilde{\rho}_p$. The exhaust velocity, $\tilde{v}_\infty$, is not included since it diverges for finite $\tilde{g}$. Choices for $\tilde{g}$ which approach zero for increasing $\tilde{r}$ could be used, however comparison of Figs. 6 and 12 show very similar behavior for values at the critical surface for $\tilde{g}$=0 and for $\tilde{g}$=1. Thus values given for the exhaust velocity in Fig. 6 can be used to approximate those for $\tilde{g}\neq 0$. Similar results are not included for other values of $\tilde{g}$ since they are very similar to those in Fig. 12.

The aspect ratio, A, is plotted as a function of $\tilde{\rho}_p$ for various values of $\tilde{g}$ in Fig. 13. It is seen that for a given value of $\tilde{\rho}_p$ there is an approximately linear relationship between $\tilde{g}$ and A. This can be seen by the combination of Eqs. (29) and (34) to give

$$A = \frac{\tilde{r}_p \; \tilde{\rho}_p \; \tilde{g}}{\tilde{P}_p} \qquad (35)$$

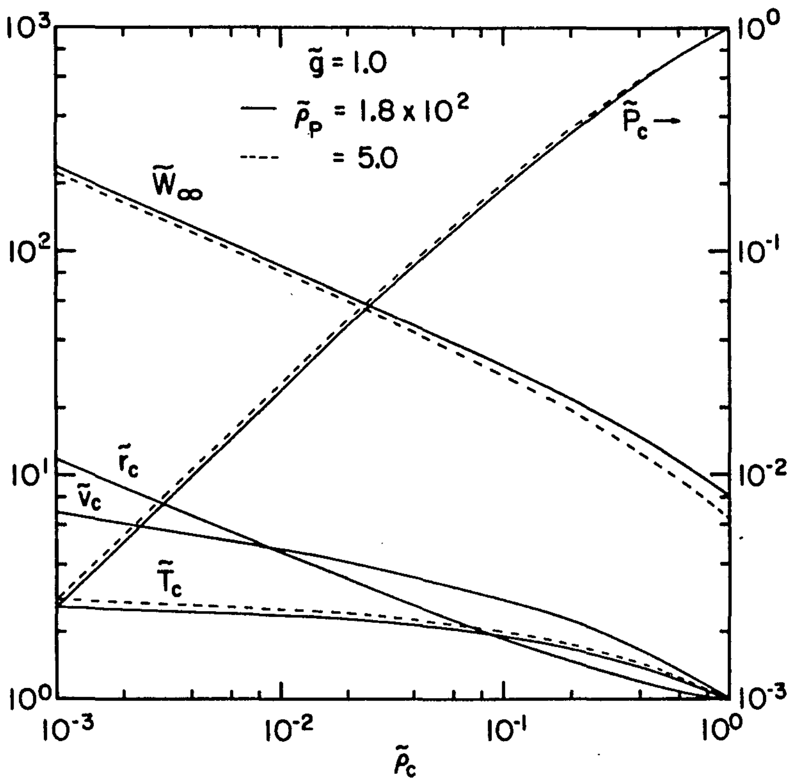

Figure 12. The dimensionless laser power and scaled flow variables at the critical surface for $\tilde{g}$=1.

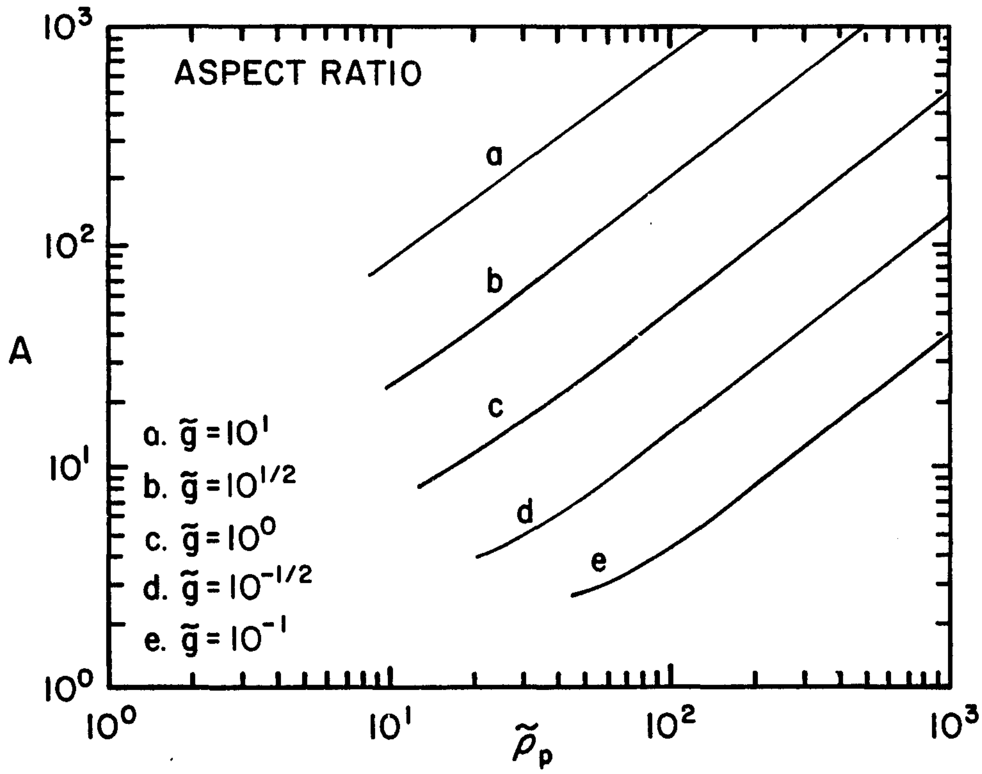

Figure 13. The aspect ratio, A, for a range of values of $\tilde{g}$.

Note that for a given value of $\tilde{\rho}_p$ there is an approximately linear relationship between $\tilde{g}$ and A.

This is approximately linear in $\tilde{g}$ for a given value of $\tilde{\rho}_p$ since $\tilde{r}_p$ and $\tilde{P}_p$ are weak functions of $\tilde{g}$. Figure 13 shows that reasonably large aspect ratios can result from values of $\tilde{g} \lesssim 1$. In these cases the shells are thin enough to neglect the effects of spherical divergence in calculating the acceleration (see Eq. 34), but at the same time spherical effects must be included in determining the ablation pressure which drives the acceleration (as previously discussed). Thus large aspect ratios do not imply that spherical effects can be neglected. This is further illustrated in the section on $\tilde{g} \to \infty$.

Range of Validity of the Solutions for Shells

The second sonic point, $\tilde{r}_{s2}$, which is located within the pellet is taken to be the inner radius of the shell. While the pressure at this point should be zero, it is seen from Figs. 7 and 8 that this is not the case. In order that this finite pressure not have a significant effect on the inward acceleration or structure of the shell it should be as small as possible. A measure of this pressure expressed as the ratio of the ablation pressure, $\tilde{P}_p$, to the pressure at the inner radius of the shell, $\tilde{P}_{s2}$, (i.e., the ratio is P_p/P_{s2}) is given in Fig. 14 for various values of $\tilde{g}$. For the assumption of steady flow to be valid, i.e., the effect of the outward flow from within the pellet be negligible, the ratio P_p/P_{s2} for any particular solution should be as large as possible. It is felt that reasonable results are obtained for $P_p/P_{s2} \gtrsim 4$. Of course if greater accuracy is desired a value greater than 4 could be chosen. For example reference to Fig. 14 shows that valid results are obtained

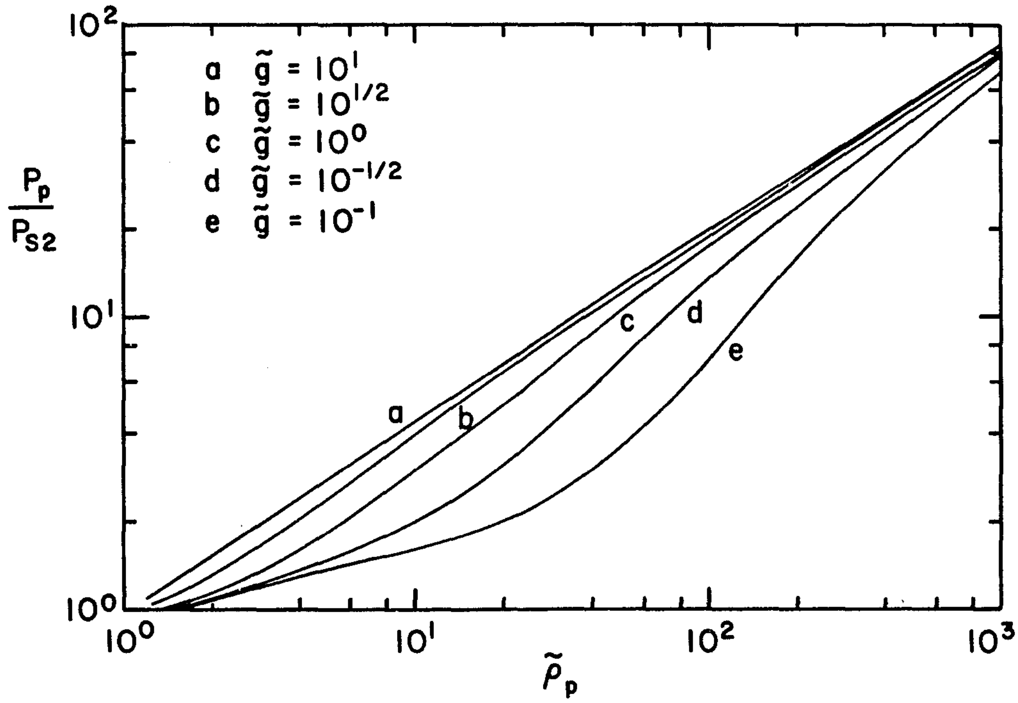

Figure 14. Ratio of the ablation pressure to that at the inner sonic point.

This ratio serves as a measure of the validity of the steady flow model for various values of $\tilde{\rho}_p$ and $\tilde{g}$. Solutions whose value of this ratio is greater than about 4 are considered reasonable.

for $\tilde{\rho}_p > 10$ when $\tilde{g}$=10 and for $\tilde{\rho}_p > 50$ when $\tilde{g}$=0.1. When dealing with solid pellets, i.e., $\tilde{g}$=0, the restriction on P_p/P_{s2} does not apply since there exists an appreciable density and pressure throughout the pellet.

Implosion Performance

The burn through parameter, B, is shown in Fig. 15 as a function of $\tilde{\rho}_p$ for various values of $\tilde{g}$. For a given value of $\tilde{g}$ it is seen that B approaches a constant value for larger values of $\tilde{\rho}_p$. This asymptotic value can be found from Eq. (32), the expression for B, and by assuming the shell can be treated as a sheet mass and using the equation of motion, Eq. (33), to give

$$B \cong \left(\frac{\tilde{g}}{\tilde{r}_p{}^2 \tilde{P}_p}\right)\left(\frac{2\tilde{r}_p}{\tilde{g}}\right)^{\frac{1}{2}} \tag{36}$$

For a fixed value of $\tilde{g}$, as $\tilde{\rho}_p$ increases to larger values both $\tilde{r}_p$ and $\tilde{P}_p$ become approximately constant (see Figs. 9, 10 and 11) and B becomes constant. This asymptotic value of B can be related to the aspect ratio, A, by combining Eqs. (35) and (36)

$$B \cong \frac{A}{\tilde{r}_p{}^3 \tilde{\rho}_p}\left(\frac{2\tilde{r}_p}{\tilde{g}}\right)^{\frac{1}{2}} \tag{37}$$

where it is remembered that this approximation applies only for large $\tilde{\rho}_p$.

A composite of Figs. 13 and 15 is presented in Fig. 16 in which B is plotted as a function of A for constant $\tilde{\rho}_p$ and for constant $\tilde{g}$. As discussed in Chapter 3 if limits are placed on B, say $0.5 \leqslant B \leqslant 1$, then

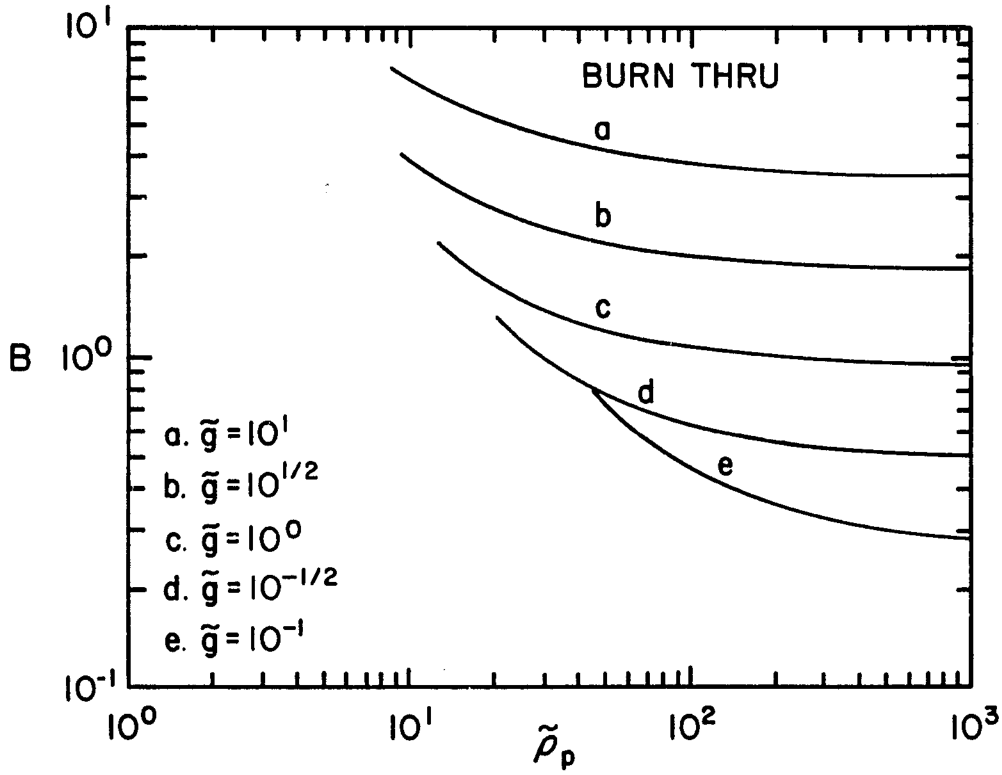

Figure 15. The burn through parameter, B, for various values of $\tilde{g}$.

This parameter is a measure of the amount of mass removed from the pellet by ablation. The most efficient transfer of energy from the incident laser to the imploded shell occurs for B just less than 1.

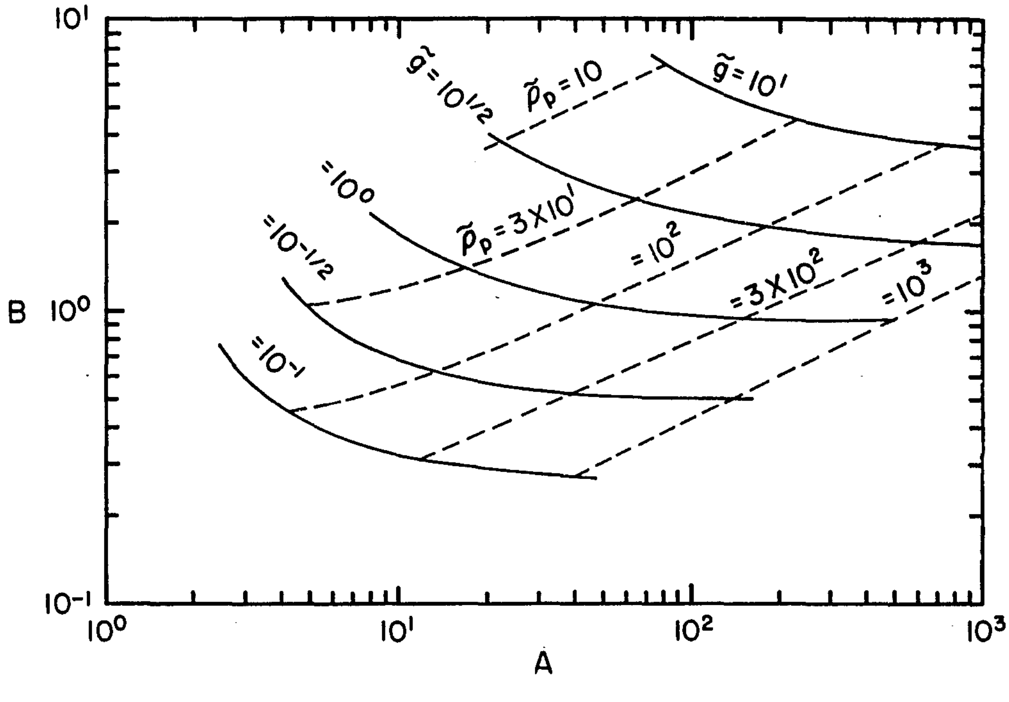

Figure 16. A composite plot of the burn through parameter and aspect ratio for constant $\tilde{\rho}_p$ and for constant $\tilde{g}$.

the region of interest for $\tilde{\rho}_p$ and $\tilde{g}$ is immediately identified. If further restraints are placed on the aspect ratio, say for reasons of hydrodynamic stability, then the region of interest becomes further restricted.

$\tilde{g} \to \infty$

A plot of a spatial profile for the planar system is given in Fig. 17 for the case $\tilde{\rho}_p=10^2$. As a comparison the case $\tilde{\rho}_p=10^2$, $\tilde{g}=1$ is shown in dashed lines in units of $\tilde{x}_g$. While the thickness of these two shells is comparable, the distance between the shell surface and the sonic point is greater and there is more mass in the ablation region for the planar case. As expected the ablation pressures are different; the effect of spherical divergence is seen for $\tilde{g}=1$ while the case $\tilde{g} \to \infty$ represents the limit of no spherical effects. Values at the pellet surface are given in Fig. 18; this plot should be compared to Figs. 9, 10 and 11. Likewise, Fig. 19 which presents quantities at the critical density should be compared to Fig. 12.

Charged Particle Beam Driven Ablation

Solutions for charged particle beam driven ablation are found by solving Eqs. (7), (8) and (13). The results that follow are for solid pellets, i.e., $\tilde{g}=0$. While solutions exist for $\tilde{g}\neq 0$, any qualitative differences from laser driven ablation can be illustrated by the $\tilde{g}=0$ case. Three different cases are shown each with $\tilde{\rho}_p=10^2$. Figure 20 illustrates a case where the beam does not penetrate to the sonic point. For this case the beam terminates at about $\tilde{r}_R=1.3$ and the charged particle

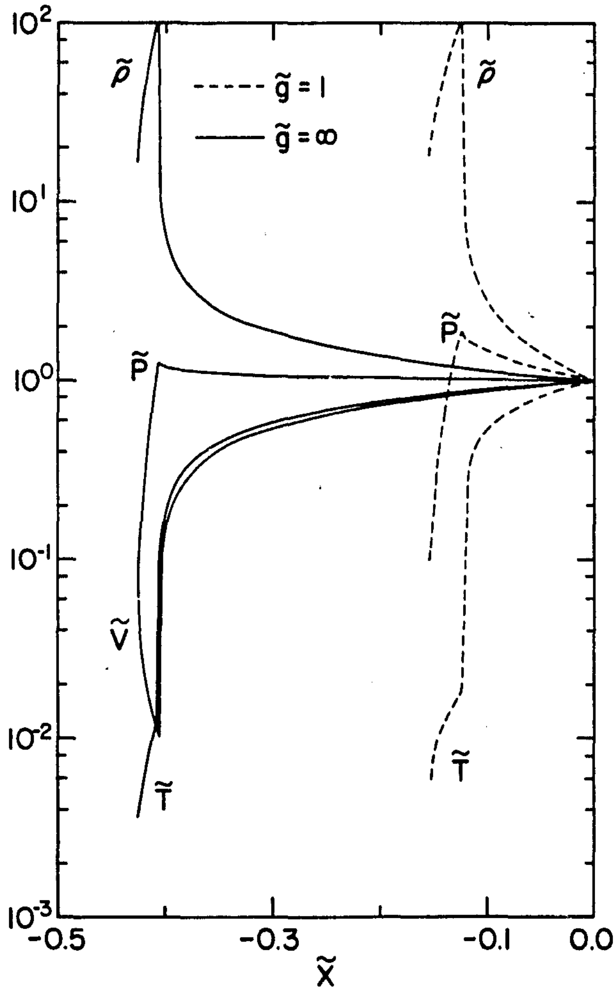

Figure 17. Profiles for $\tilde{\rho}_p = 10^2$ and $\tilde{g} \to \infty$.

A comparison case of $\tilde{\rho}_p = 10^2$, $\tilde{g} = 1$ in units of $\tilde{x}_g$ is also included. While the thickness of these two shells is comparable, the overall structure and ablation pressures are quite different.

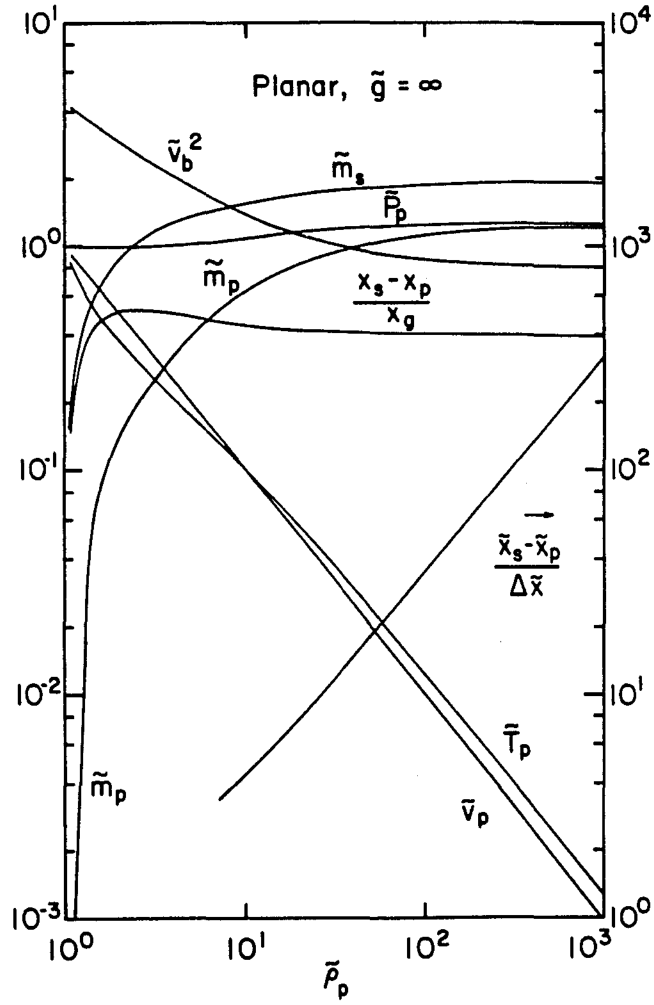

Figure 18. Various values at the pellet surface and sonic points for the planar case.

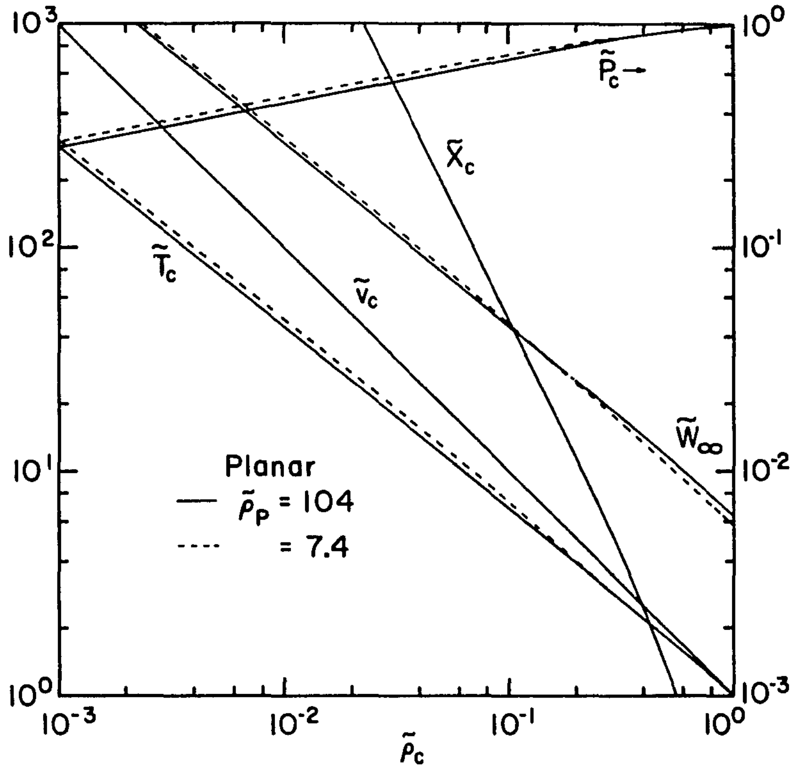

Figure 19. Critical surface values and laser power for the planar case.

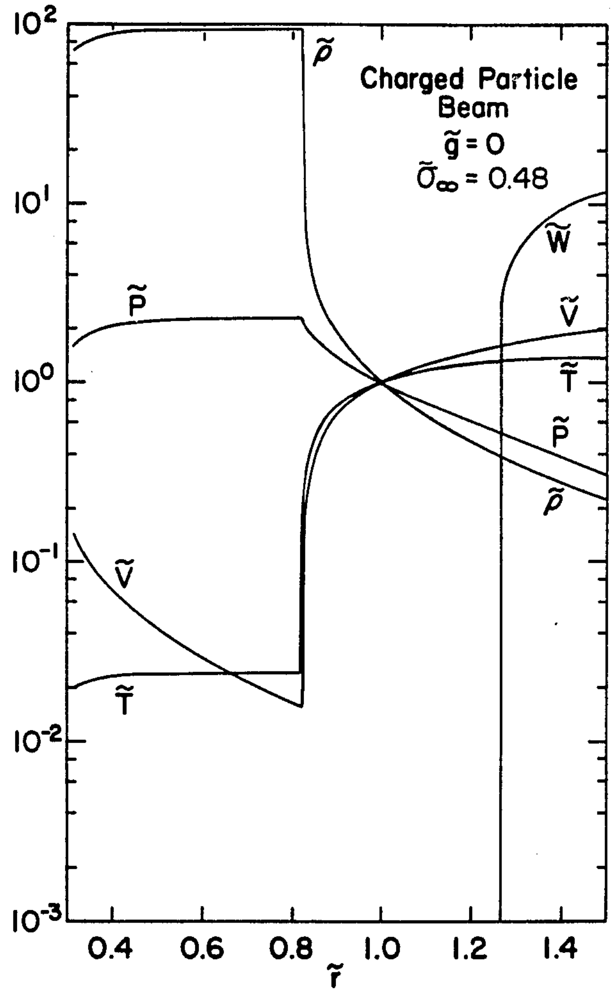

Figure 20. Logarithmic profiles of charged particle beam deposition case for $\rho_p=10^2$, $\tilde{g}=0$ and $r_R>r_s$.

Note that the particle beam does not penetrate into the subsonic region.

range is $\tilde{\sigma}_\infty$=.48. The solution of $\tilde{r} < \tilde{r}_R$ is identical to that of laser deposition with $\tilde{r}_c$=1.3 since the inward energy flow for both cases is by thermal conduction. Figures 21 and 22 present profiles in which the termination point of the particle trajectories is within the sonic radius at about $\tilde{r}_R$=.97 and .93 and have values of $\tilde{\sigma}_\infty$=.81 and .93, respectively. In Fig. 21 thermal conduction is still important for the inward flow of energy, but in Fig. 22 this is not the case. The beam penetrates right up to the pellet's surface at about $\tilde{r}_R$=.93 and the inward energy flow is transported by the beam. This latter case is an example of the behavior described by Eq. (19) in which heat flow plays a very limited role.

Various quantities of interest for charged particle beam driven ablation are shown as functions of the range, $\tilde{\sigma}_\infty$, in Fig. 23. This plot contains $\tilde{W}_\infty$, $\tilde{v}_\infty$ and $\tilde{W}_s$ and is analogous to Fig. 6. Similar to the case of laser driven ablation, where $\tilde{W}_\infty$ is seen to increase with increasing $\tilde{r}_c$, $\tilde{W}_\infty$ increases with increasing $\tilde{r}_R$ since the deposited energy must be transferred further through outward flowing material to reach the ablation surface. Also, $\tilde{W}_\infty$ increases faster than $\tilde{v}_\infty^2$ with increasing $\tilde{r}_R$ due to the finite outward heat flow as $r \to \infty$ (this can be seen from the asymptotic solutions, Eqs. (20), (21) and (22)).

Values of $\tilde{\sigma}_\infty$ greater than about .7 correspond to cases in which the particle trajectories penetrate within the sonic radius. This occurs where $\tilde{r}_R < 1$ and $\tilde{W}_s > 0$. For the two very different values of $\tilde{\rho}_p$ used in in Fig. 23 it is seen that the largest possible value of range is $\tilde{\sigma}_\infty \cong 1$. This occurs at $\tilde{r}_R \cong \tilde{r}_p$, and corresponds to the most efficient case since

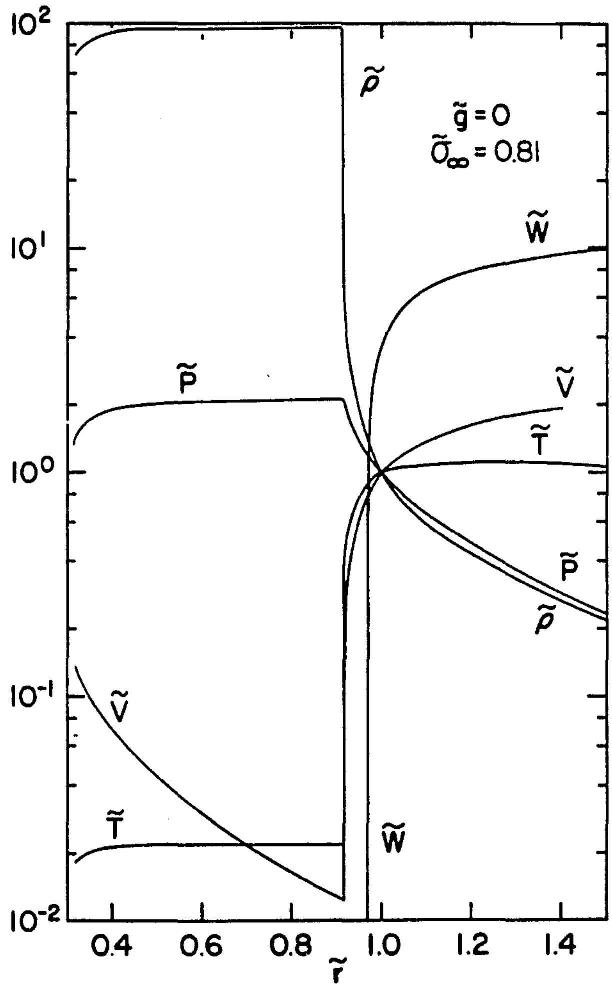

Figure 21. Particle beam penetrates within the sonic point and thermal conduction is important.

Ablation driven by charged particle beam where the beam penetrates within the sonic point. Thermal conduction is still important for this case.

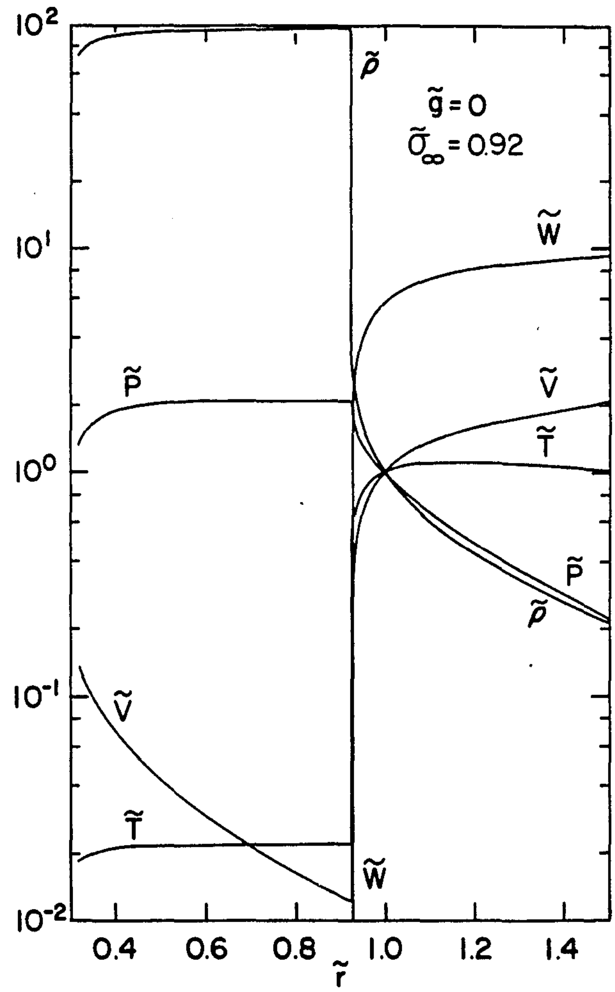

Figure 22. Ablation profiles where thermal conduction plays a very limited role.

The energy of the particle beam is converted directly to kinetic energy.

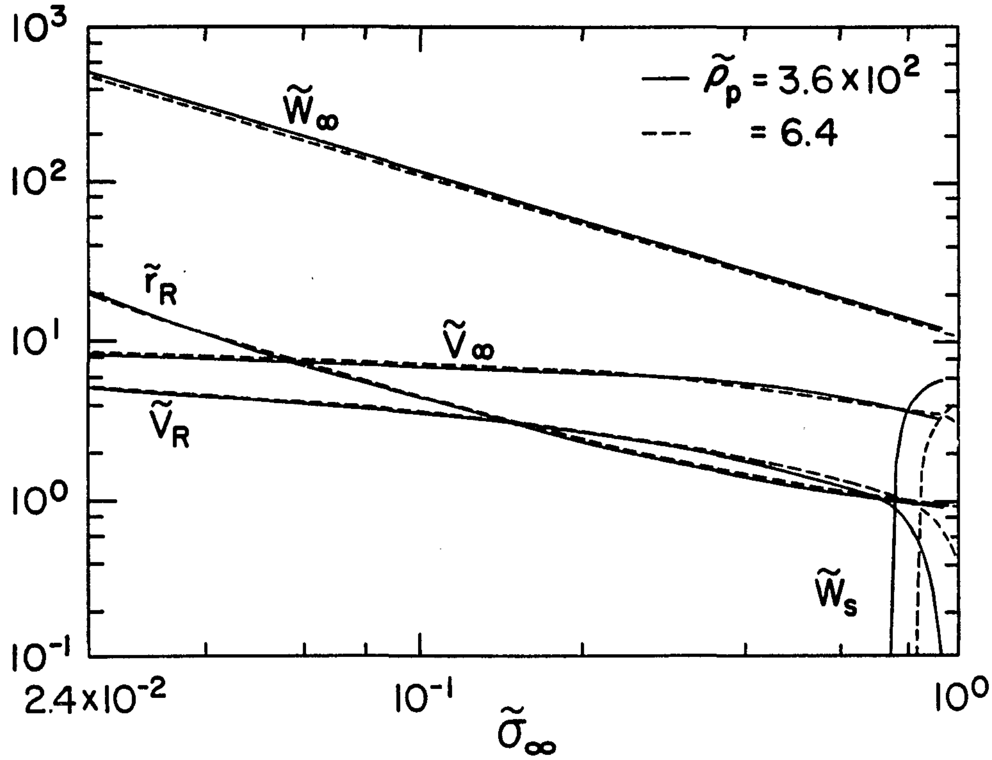

Figure 23. Scaled particle beam power and other computed quantities as a function of the range, $\tilde{\sigma}_\infty$.

This plot is analogous to Fig. 6.

the least power is needed to drive the ablation. If $\tilde{\sigma}_\infty$ is still increased further for a given value of $\tilde{\rho}_p$, then the flow no longer corresponds to ablation and the pellet has burnt through.

CHAPTER 5

DESCALING AND CONCLUSIONS

In order to compare the results of the steady flow model to either experiment or numerical simulation, it is helpful to transform the dimensionless quantities to dimensional results. A procedure for descaling the results for a solid pellet driven by laser energy deposition is presented. This same procedure is also applicable to shell solutions. Examples of descaled results for both of these cases are presented.

The Descaling Procedure

First the pellet material, inflight radius, r_p, and peak density, ρ_p, are chosen. The choice of pellet material determines the gas constant, R, as well as the coefficient, G(Z), which is proportional to the thermal conductivity. The critical density, ρ_c, is determined by the laser light frequency. At this point G(Z), ρ_p, ρ_c, r_p and R are determined and can now be used to descale the results of the steady flow model.

A value for $\tilde{\rho}_p$ in the range of interest, say $10 \leqslant \tilde{\rho}_p \leqslant 10^3$, is chosen. It is recalled that for each value of $\tilde{\rho}_p$ there is a corresponding value of M, $\tilde{r}_p$, $\tilde{P}_p$ and other scaled values at the pellet surface (see Fig. 5). Since ρ_p and r_p are known, ρ_s and r_s are determined for this particular choice of $\tilde{\rho}_p$. T_s is found from M using the last relationship of Eq. (9). Since $v_s=(RT_s)^{\frac{1}{2}}$ all quantities at the sonic point are now given.

The next step is to determine the quantities of interest at the critical radius, r_c. Since ρ_s and ρ_c are known this determines $\tilde{\rho}_c$. This together with M can be used to find the scaled ablation power, $\tilde{W}_\infty$, and scaled flow quantities at $\tilde{r}_c$ from results similar to Fig. 6 or by direct solution of Eqs. (7), (8) and (12). The ablation power, W_∞, is now determined from $W=Sv_s^2\tilde{W}/2$.

This now completes the procedure giving the flow quantities at the ablation surface, sonic point and critical radius as well as the ablation power. These same steps are repeated for other choices of $\tilde{\rho}_p$ to obtain a wide range of values of descaled results.

Descaled Results

The results of this descaling process are seen in the next three figures. The target material is carbon and the pellet radius is 100 μm with a pellet density of 4 g/cm^3 which could result from an initial solid density of 1 g/cm^3 multiplied by a shock jump ratio of 4. The mass ablation rate, temperatures at the sonic radius and pellet surface, ablation pressure and electron number density at the sonic point, n_{es}, are plotted as a function of the ablation power given in watts. The laser irradiance, F_c, which is a measure of incident laser power per unit area is included and is defined as $F_c=W/(4\pi r_c^2)$. Figures 24 and 25 correspond to solid pellets, i.e., $\tilde{g}=0$, with the ablation driven by 1.06 μm laser light (this corresponds to an electron number density, n_{ec}, of

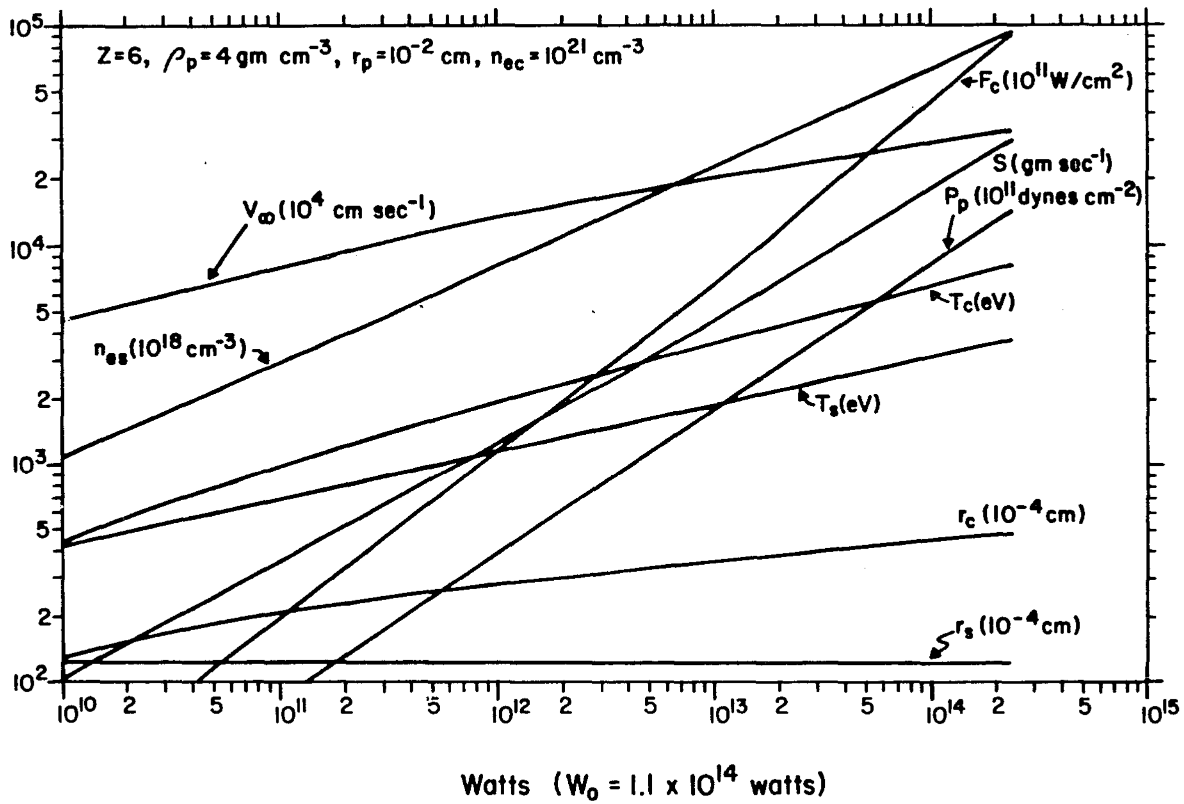

Figure 24. Descaled results from the steady flow model for ablation driven by 1.06 μm laser light.

The minimum power on this plot corresponds to where the sonic and critical surfaces coalesce.

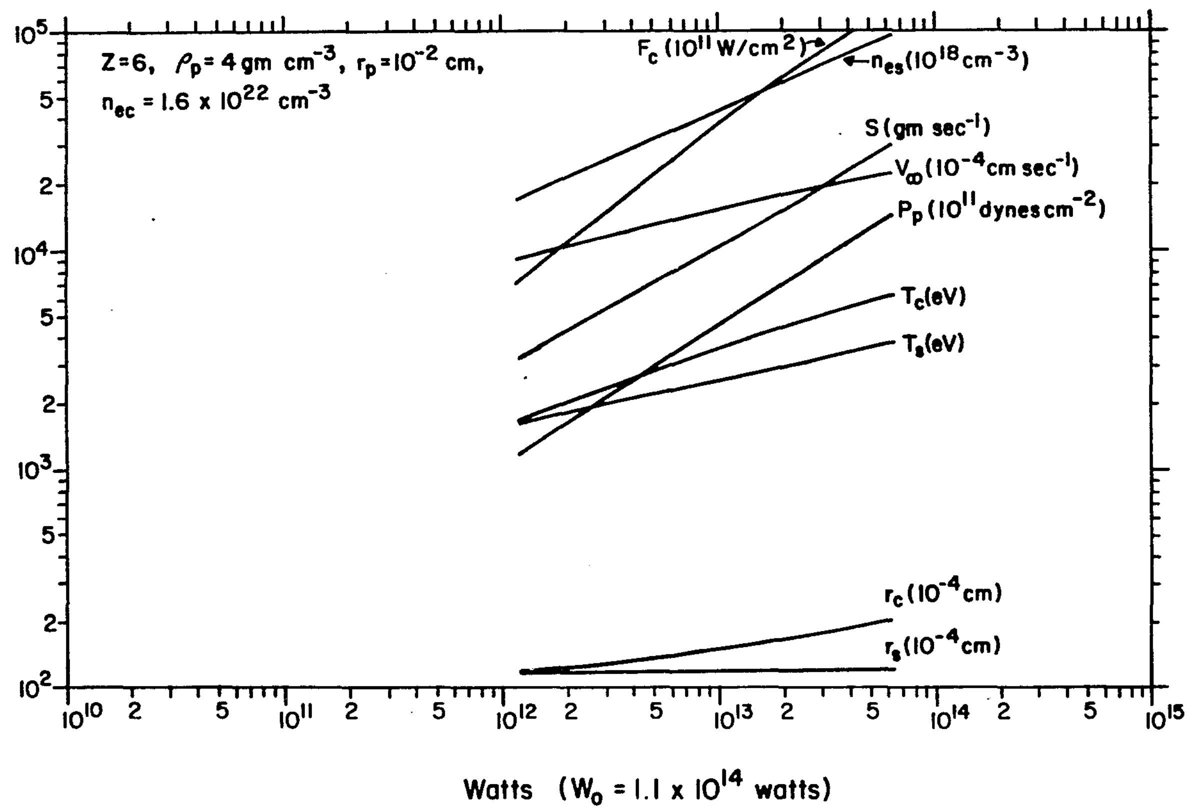

Figure 25. Descaled results for ablation driven by frequency quadrupled 1.06 μm light.

This plot and the next plot are drawn to the same scale as the previous plot to emphasize how the power necessary to drive ablation changes. It is seen that the power at which the sonic and critical surfaces coalesce is larger than for the 1.06 μm case.

10^{21} cm^{-3}) and frequency quadrupled 1.06 μm light (n_{ec}=$1.6x10^{22}$ cm^{-3}), respectively. The exhaust velocity is also included on these plots. The largest power on each plot ($2.3x10^{14}$ and $6.4x10^{13}$ watts for Figs. 24 and 25, respectively) roughly corresponds to burn through, i.e., $\tilde{\rho}_p \cong 10$. By comparing these plots it is seen that the power is proportional to $\rho_c^{-1/2}$ as described in McCrory and Morse (1977) for a constant set of implosion parameters (e.g., constant P_p). On each plot the minimum power occurs where the sonic and critical surfaces coalesce. This occurs at a much lower power for the case of 1.06 μm light. Results for other values of Z, the atmoic number, have been obtained which show that for increasing Z (i.e., decreasing G(Z)) that both ρ_s and the mass flow rate, S, decrease for a given set of pellet parameters and constant laser power. Since less material is removed for a given laser power, that which is removed must convect away a larger energy per unit mass, thus T_s and v_∞ increase. For a given set of constant implosion parameters but with targets composed of different Z materials, v_∞ is roughly proportional to $Z^{0.1}$ while S is roughly proportional to $Z^{-0.1}$. Results for a shell ($\tilde{g}$=1) driven by frequency quadrupled 1.06 μm light are presented in Fig. 26. The aspect ratio is also included which is seen to decrease with increasing power.

Generalized Scaling of Descaled Results

A convenient method of representing the descaled results for a large range of pellet parameters, laser wavelengths and deposited powers is by introduction of the following scaling factors. The power is scaled according to W_o, where

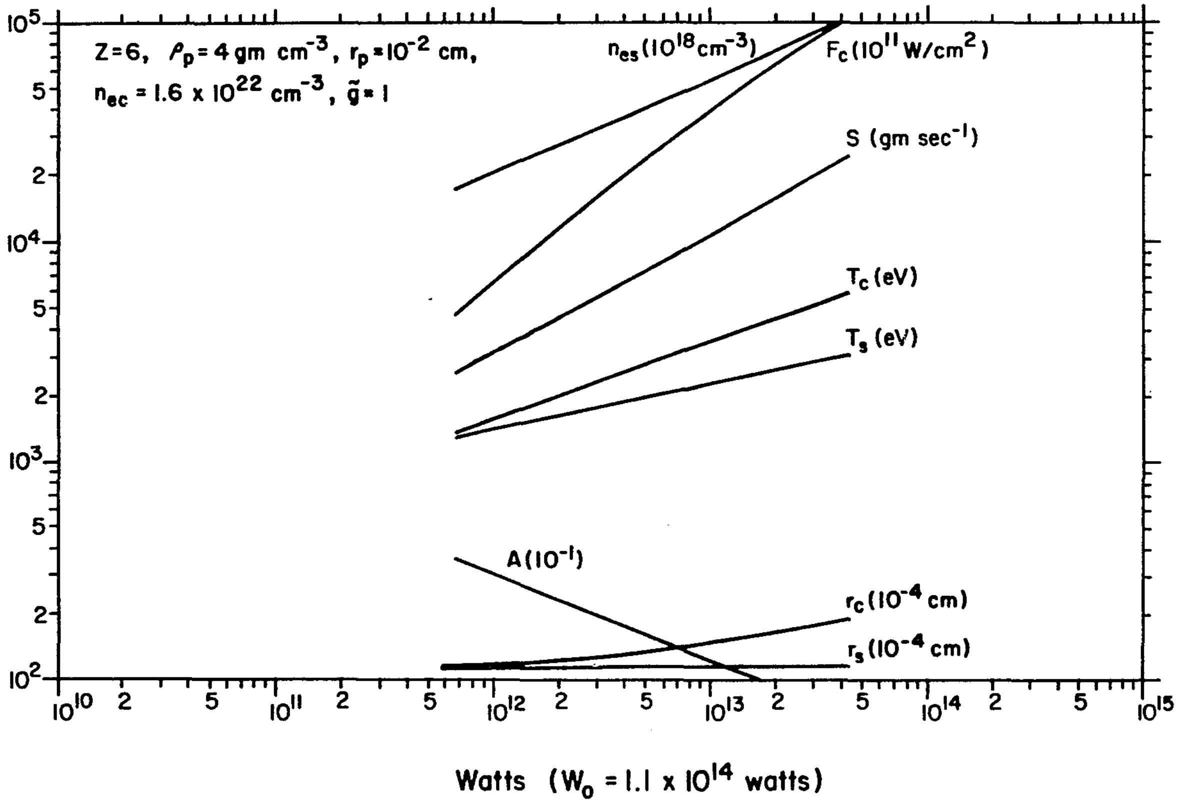

Figure 26. Descaled results for shell solution, $\tilde{g}$=1, driven by 1.06 μm laser light.

$$W_o = 2\pi r_p^{\,2} \rho_p R^{3/2} \left(\frac{\rho_p \, r_p \, R^{3/2}}{G(Z)} \right)^{\frac{3}{2\alpha-1}}$$

which is determined by the choice of pellet material, density and radius. Likewise a scaling temperature, T_o, is defined

$$T_o = \left(\frac{\rho_c \, r_p \, R^{3/2}}{G(Z)} \right)^{\frac{1}{\alpha-\frac{1}{2}}}$$

whose corresponding velocity, v_o, is $v_o = (RT_o)^{\frac{1}{2}}$. These quantities are determined by the target material, pellet radius and laser wavelength. These scaling quantities are obtained as a result of scaling Eqs. (1), (2) and (3) in terms of ρ_p, r_p and ρ_c.

Results for solid carbon pellets are shown in Fig. 27 for a wide range of values of the ratio ρ_p/ρ_c. The sonic density scaled to the critical density, ρ_s/ρ_c, the temperature at the sonic point, T_s/T_o, and the scaled sonic velocity, v_s/v_o, are shown. Similar results for the same values of the ratio ρ_p/ρ_c, but for carbon shells with g=1 are found in Fig. 28. The aspect ratio is included on this plot in order to uniquely identify solutions for shells, since when comparing these results to either experimental results or numerical simulations the aspect ratio and deposited power must match. Both of these figures cover a range of values of W/W_o from $W/W_o=10$, where $\rho_c=\rho_s$, increasing until burn through occurs.

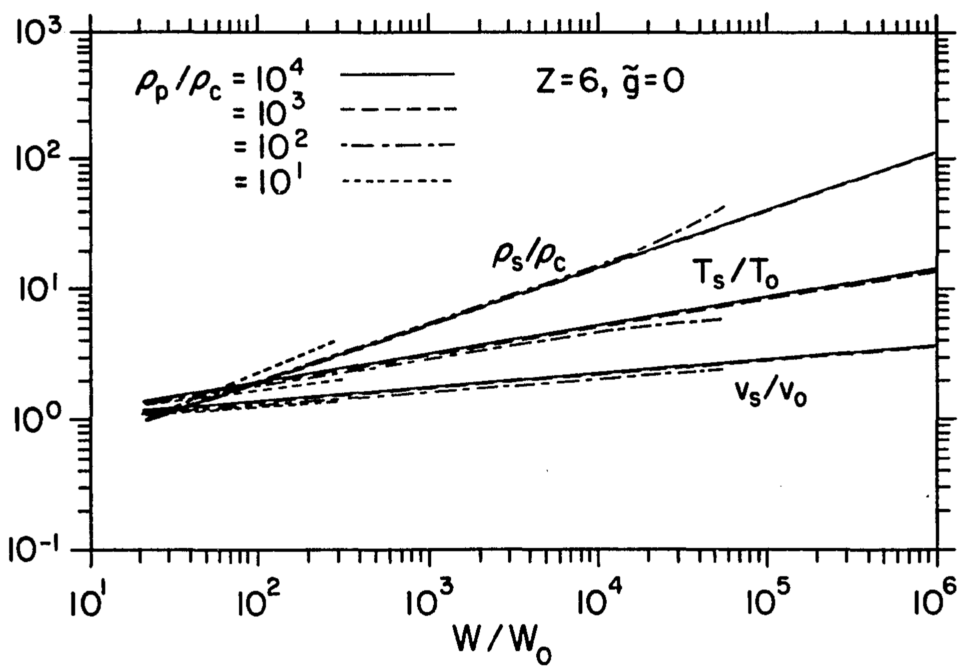

Figure 27. A set of descaled results for a wide range of values of the ratio $\tilde{\rho}_p/\tilde{\rho}_c$ for $\tilde{g}$=0.

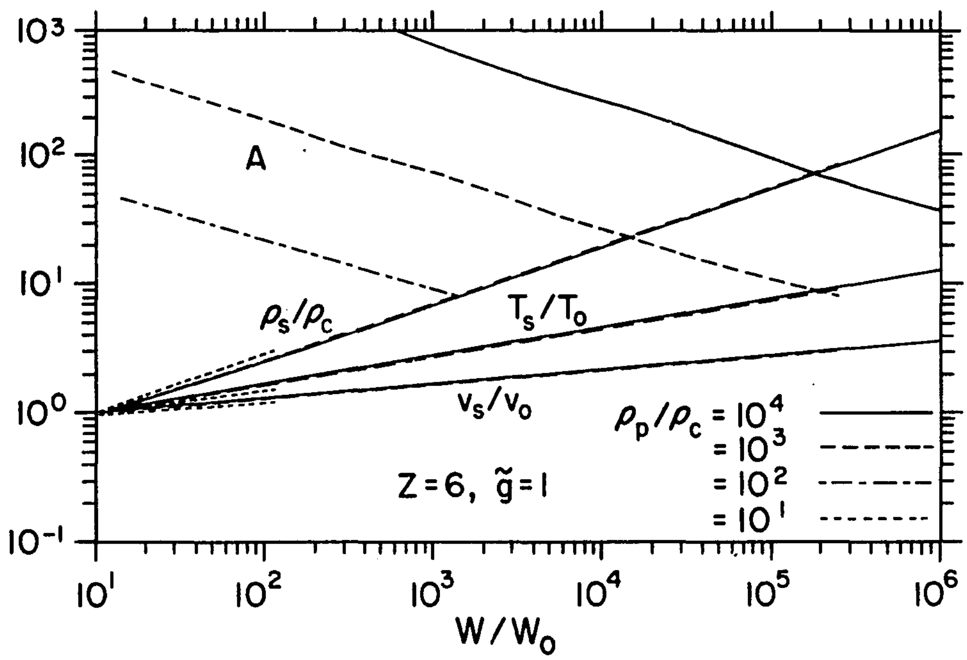

Figure 28. A range of descaled results for $\tilde{g}$=1.

The aspect ratio is also included.

Results for Inverse Bremsstrahlung

The model of energy deposition by inverse bremsstrahlung (see Appendix A) can be used to investigate the behavior of solutions for which $\rho_c > \rho_s$. In this case the descaling process is more complicated since an additional parameter, M_2, is involved. This additional parameter restricts the number of parameters which can be assumed (these are ρ_p, r_p, Z and A in the cases just considered) by one. In this procedure these same parameters are specified except for the pellet density. It is determined by taking the ratio of M to M_2, thus eliminating r_s, and solving for ρ_s; since $\tilde{\rho}_p$ is also known this determines ρ_p. Various solutions are investigated until the desired value of ρ_p is found. This procedure is repeated for various values of $\tilde{\rho}_p$. An example of descaled results are seen in Fig. 29 for the same parameters as in Fig. 25. This represents a range of values of $\tilde{\rho}_c$ from 0.5 to 10. Which gives a continuation of descaled results for values of $\rho_c > \rho_s$. Reference to these two plots shows that as the laser power decreases ρ_s decreases until $\rho_s = \rho_c$, ρ_s further decreases for decreasing laser power. For the given parameters $\rho_s = \rho_c$ at a power of about 1.1×10^{12} watts.

Conclusion

Solutions for spherical shell-like targets are presented for several values of the acceleration parameter $\tilde{g}$. In the limit that the acceleration effects due to $\tilde{g}$ become much larger than spherical divergence effects the system becomes planar. While these planar solutions appear to be a simplifying approximation to large aspect ratio shells, it is

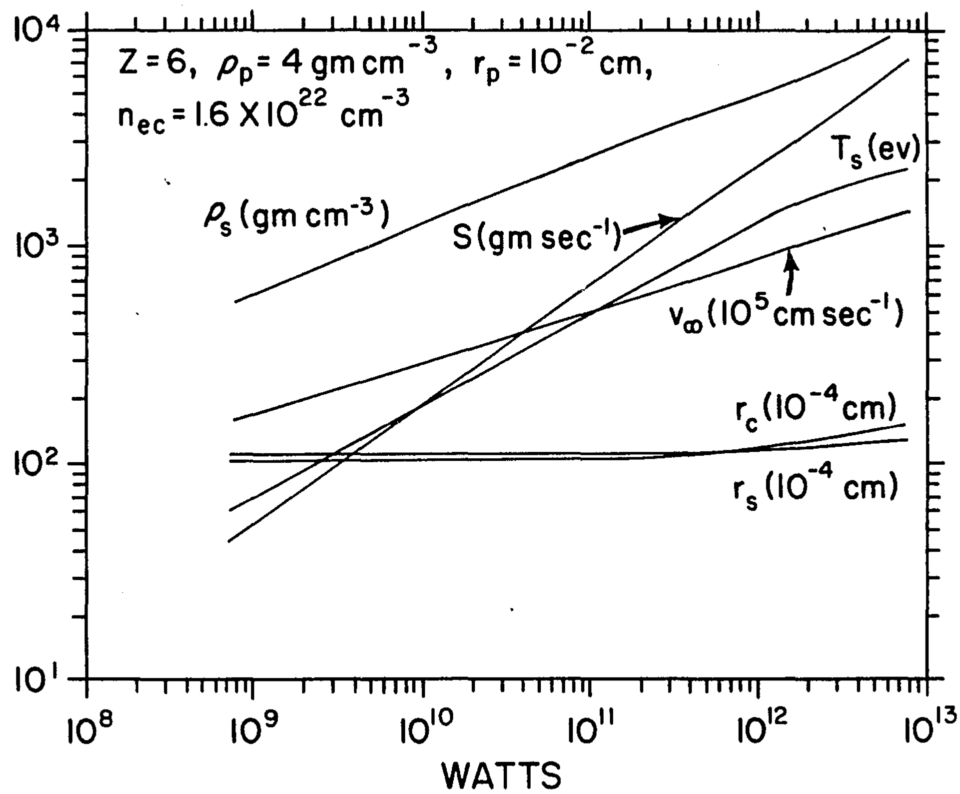

Figure 29. Descaled results from the inverse bremsstrahlung model for $\rho_c > \rho_s$.

This includes a range of values of $\tilde{\rho}_c$ from 0.5 to 10.

seen that the ablation pressures for these two cases can be quite different. Thus this simplification neglects spherical divergence effects which can be important for large aspect ratio shells.

A measure of the hydrodynamic efficiency of imploding shells can be presented by the burn through parameter, B, a function of the scaled peak density, $\tilde{\rho}_p$, aspect ratio, A, and acceleration, $\tilde{g}$. A wide range of solutions with acceptable values of B are presented such that they can be easily identified and should provide a useful reference to workers in the field. Once the desired scaled solutions are found the procedure in the last section may be used to descale them.

Models are presented for ablation driven by charged particle beam deposition and for laser energy deposition by inverse bremsstrahlung. Solutions for these two models are presented. These include an interesting case in which thermal conduction plays an unimportant role in inward energy transport. The inverse bremsstrahlung deposition model is particularly useful for investigation cases where ρ_c is greater than ρ_s.

The descaling procedure can be used to obtain scaling laws as well as readily compare the results of the steady flow model to either experiment or numerical simulation.

APPENDIX A

ENERGY DEPOSITION BY INVERSE BREMSSTRAHLUNG

The deposition of laser energy by inverse bremsstrahlung is a useful addition to the steady flow model since it allows solutions for $\rho_c > \rho_s$. In this model the power loss per unit length due to inverse bremsstrahlung is given by

$$\frac{dW}{dr} = W \kappa_\nu (c/v_g) \tag{A1}$$

where c is the speed of light, v_g, the group velocity is given by $v_g = c(1-\rho/\rho_c)^{\frac{1}{2}}$ and the absorption coefficient κ_ν is given by Spitzer to be

$$\kappa_\nu = \frac{4}{3} \left(\frac{2\pi}{3kT}\right)^{\frac{1}{2}} \frac{Z^3 n_i^2 e^6}{hc\, m_e^{3/2} \nu^3} \left(1 - e^{-h\nu/kT}\right) g_{ff}$$

where n_i is the ion number density, e, the electron charge, m_e, the electron mass, ν, the laser frequency and h is the Planck constant. The Gaunt factor, g_{ff}, is taken to be one in what follows. After rearranging terms, scaling to the sonic point and since $h\nu >> kT$, Eq. (A1) becomes

$$\frac{d\tilde{W}}{d\tilde{r}} = \frac{M_2 \tilde{W} \tilde{\rho}^2}{\tilde{T}^{3/2}(1-\tilde{\rho}/\tilde{\rho}_c)^{\frac{1}{2}}} \tag{A2}$$

where

$$M_2 = \frac{M'}{\tilde{\rho}_c} = \frac{4}{3} \left(\frac{2\pi}{3k^2 T_s^3}\right)^{\frac{1}{2}} \frac{Z^2 e^4 \rho_s^2 N_o g_{ff} r_s}{c\, m_e^{\frac{1}{2}} A \rho_c}$$

and

$$M' = r_s \kappa_{\nu s} = r_s/L_{As}$$

where $L_{As} \equiv$ absorption length at the sonic point. The boundary condition for Eq. (A2) is that $\widetilde{W}=\widetilde{W}_c$ at $\widetilde{\rho}=\widetilde{\rho}_c$. Details of the solution procedure require that $\widetilde{W}_c$ is found by requiring $\widetilde{T}\to 0$ as $\widetilde{r}\to\infty$. The equations which are solved are Eqs. (7), (A2) and the following energy equation

$$\frac{d\widetilde{T}}{d\widetilde{r}} = M \frac{(\widetilde{v}^2-\widetilde{v}_b{}^2)/2 + \eta\widetilde{T} - \tfrac{1}{2}(\widetilde{W}_I-\widetilde{W}_R)}{\widetilde{r}^2\,\widetilde{T}^{\alpha}} \tag{A3}$$

where $\widetilde{W}_I$ and $\widetilde{W}_R$ are the power of the incident and reflected beams, respectively. Integration of Eq. (A2) gives $\widetilde{W}_I$ whereas $\widetilde{W}_R$ is found by replacing M_2 by $(-M_2)$ in Eq. (A2), and as previously mentioned $\widetilde{W}_I=\widetilde{W}_R=\widetilde{W}_c$ at $\widetilde{\rho}=\widetilde{\rho}_c$. The value of the incident beam, $\widetilde{W}_\infty$, is found since $\widetilde{W}_I\to\widetilde{W}_\infty$ as $\widetilde{r}\to\infty$.

For $\widetilde{g}=0$ solutions to these equations form a three parameter family dependent upon M, M_2 and $\widetilde{\rho}_c$. As in the case of ablation driven by charged particle beams, there are two distinct types of solutions. These are $\rho_c < \rho_s$ in which case the subsonic solutions are identical to those presented in Chapter 4 for the case of laser driven ablation (function of M only), and $\rho_c > \rho_s$ where the subsonic solutions are functions of M, M_2 and $\widetilde{\rho}_c$. In this latter case the light beam penetrates within the sonic point and heat flow can play a diminished role. Equation (15) is replaced by

$$M = \frac{2(2+\tilde{g})}{1 - \tilde{v}_b^{\,2} + 2\eta - (\tilde{W}_{Is} - \tilde{W}_{Rs})} \tag{A4}$$

where $\tilde{W}_{Is}$ and $\tilde{W}_{Rs}$ are values of the power at the sonic point for the incident and reflected beams, respectively. When finding solutions of this type it becomes necessary to iterate M_2, $\tilde{W}_{Is}$ and $\tilde{W}_{Rs}$ while keeping the quantity $(\tilde{W}_{Is}-\tilde{W}_{Rs})$ constant so that $\tilde{W}_I=\tilde{W}_R$ at $\tilde{\rho}=\tilde{\rho}_c$ when finding the subsonic solutions, and also matching the temperature boundary condition as $\tilde{r}\to\infty$ for the supersonic solutions.

Examples of solutions for the case of energy deposition by inverse bremsstrahlung are seen in Figs. 30, 31 and 32. These plots are for $\tilde{g}=0$ and constant $\tilde{v}_b^{\,2}$. The first of these, Fig. 30, is for $\rho_c < \rho_s$ and energy flow between the critical and the ablation surfaces is by thermal conduction. Figure 31 illustrates a case for $\rho_c > \rho_s$ but thermal conduction is still important for energy transport. In Fig. 32, $\rho_c > \rho_s$ and the beam penetrates right up to the ablation surface. The energy of the incident laser is converted directly to convective energy and thermal conduction plays a very diminished role. This represents a case in which $\kappa_s \to 0$.

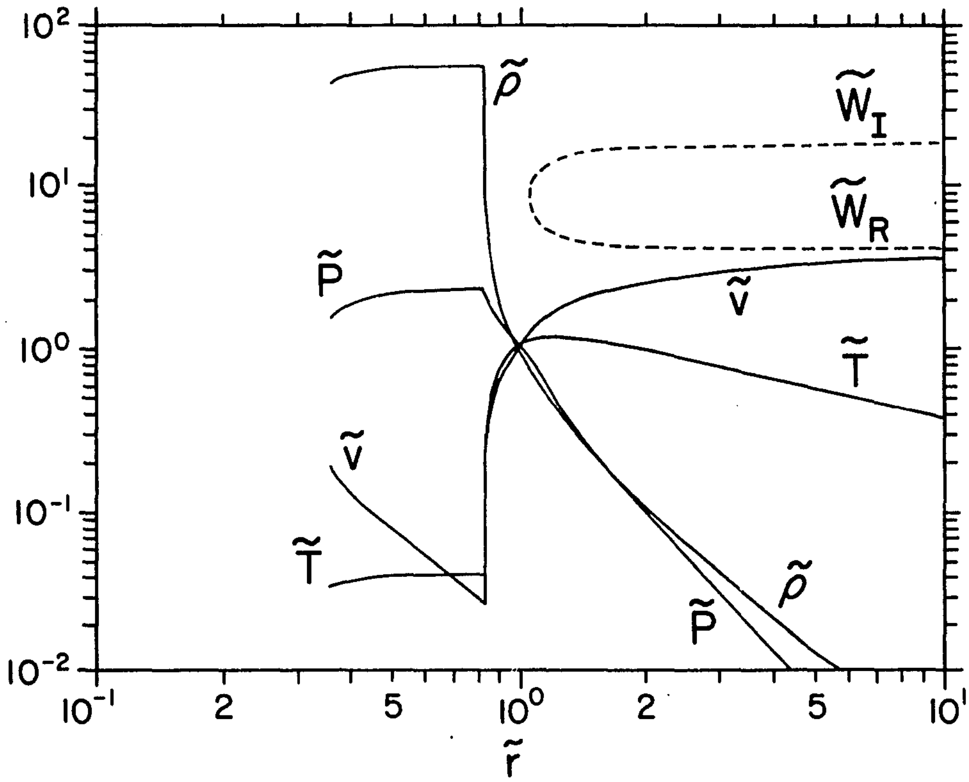

Figure 30. Profiles for inverse bremsstrahlung.

Energy flow between the critical and ablation surfaces is by thermal conduction.

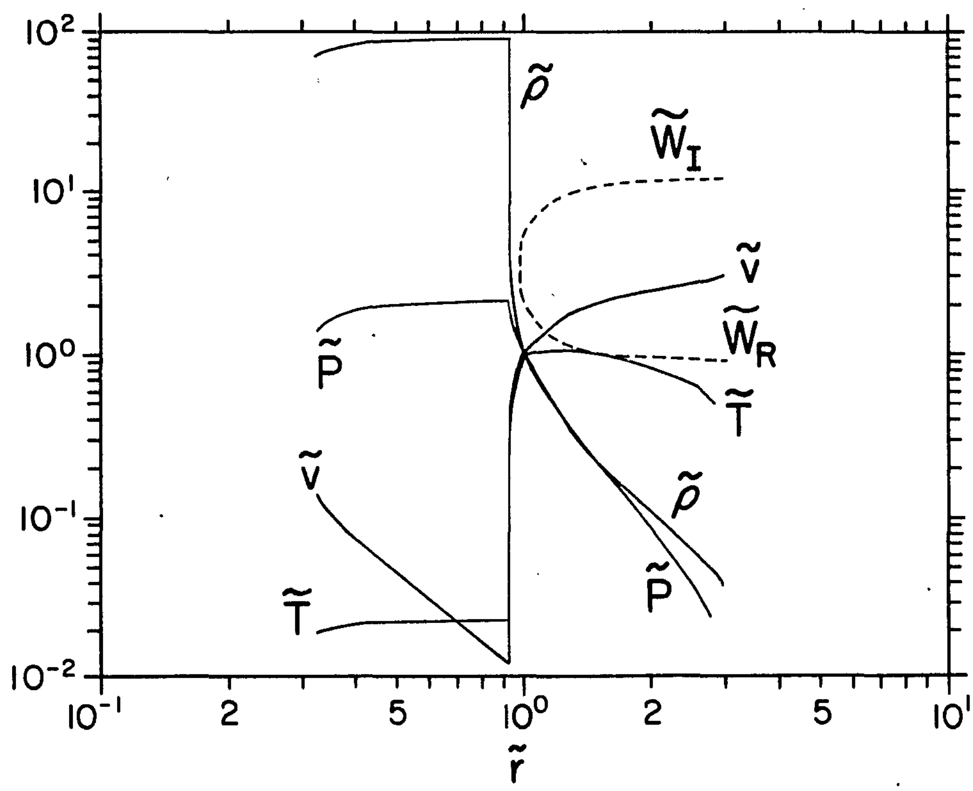

Figure 31. Laser deposition with $\rho_c > \rho_s$ and thermal conduction is important.

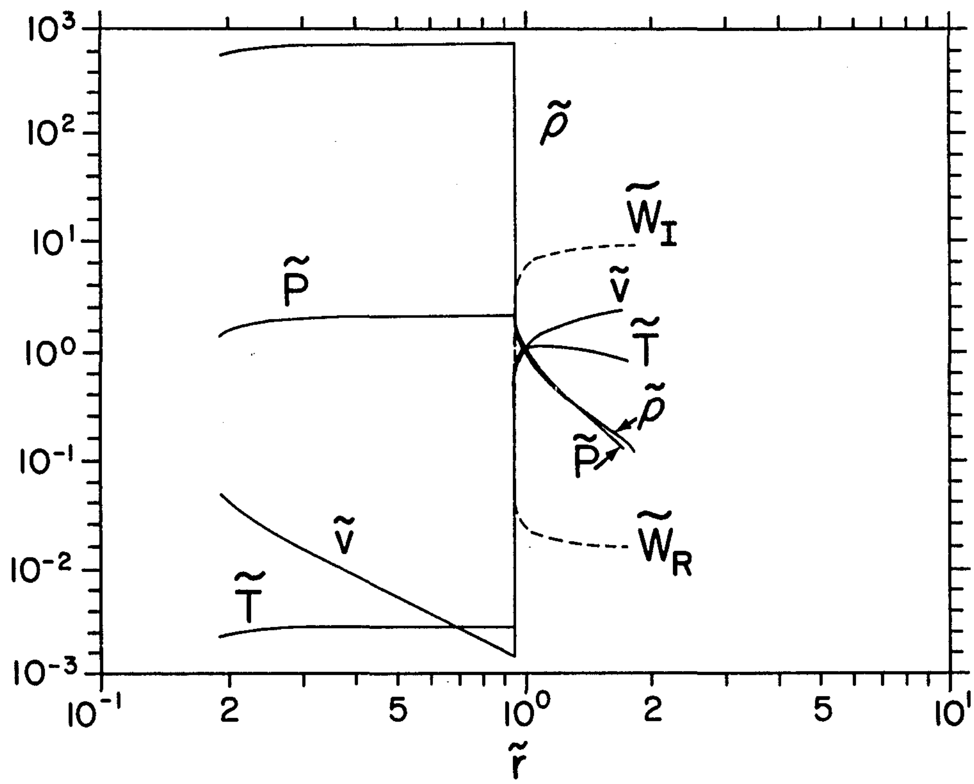

Figure 32. Thermal conduction is unimportant, $\rho_c > \rho_s$.
This represents a case in which $\kappa_s \to 0$.

REFERENCES

Bobin, J. L., Phys. Fluids 14, 2341 (1971).

Brueckner, K., Rev. Mod. Phys., April 1974.

Brueckner, K. and S. Jorna, Rev. Mod. Phys. 46, 325 (1974).

Clarke, J. S., H. N. Fisher, and R. J. Mason, Phys. Rev. Lett. 30, 89 (1973); 30, 249 (1973).

Fauquignon, C. and F. Floux, Phys. Fluids 13, 386 (1970).

Felber, F. S., Phys. Rev. Lett. 39, 84 (1977).

Gitomer, S. J., R. L. Morse, and B. S. Newberger, Phys. Fluids 20, 234 (1977).

Max, C. E., C. F. McKee, and W. C. Mead, Lawrence Livermore Laboratory Report No. UCRL-78458 (1976).

McCrory, R. L. and R. L. Morse, Phys. Rev. Lett. 38, 544 (1977).

Nuckolls, J., L. Wood, A. Thiessen, and G. Zimmerman, Nature (London) 239, 139 (1972).

Spitzer, L., Physics of Fully Ionized Gases (Interscience, New York, 1962), Chap. 5, p. 143.